DOCTORAL THESIS

Procedures of Titanium Recovery from Residual Materials Resulted in Industrial Processing of Materials with High Content of Titanium

Faculty of Applied Chemistry and Material Science

Department : General Chemistry

Scientific coordinator:
Prof. Dr. Ing.
Pîrvu Cristian Valeriu

PhD: **Moldoveanu Laura Eugenia**

București – 2021

1. Introduction

This thesis aims to reuse some waste from Romanian industry, from a factory producing titanium ingots. (Zirom SA Giurgiu).

Due to obtaining and processing procedures of titanium ingots result a type of titanium scrap (provided from the ingots surface) which can not be returned into technological process because improperly impurities content.

This work brings new directions to reuse this waste, like this: rare and relatively rare earth recovery using as retention bed titanium scrap; titanium scrap utilization for some pollutant degradation such as phenol degradation and titanium scrap usage for its antibacterial behaviour.

Another secondary product (waste) resulted due to titanium ingots processing by forging is a dusty material mixed with an abrasive material (resulted due grinding and shot blasting process applied to titanium forging products.) This waste have important contents of titanium and iron.

The aime of this work is to identify an efficient way to reuse this dust resulted from titanium ingots forging process. This waste was integrated in construction materials by partial replacing of aggregate used for motars as basis in Portland cements.

2. Investigation techniques for titanium and titanium alloys

2.1. Morphological methods of investments for titanium and titanium alloys

The morphological methods used in this work were : SEM (Scanning Electron Microscopy) and DRX (X Ray Diffraction)

2.1.1. SEM (Scanning Electron Microscopy)

Scanning Electron Microscopy is known shortly as SEM and is a facile method of sample characterization using an electron focused beam. This technique is able to view samples surface characteristics using accelerate electrons. SEM should be used: to view sample morphology, for local elemental samples composition, for cristaline structure observation and for optical and electrical samples properties [1]. Sample aria that should be scanned with such as instrument is radiated with an electrons beam finely focussed. Electrons interaction with sample give a lot of signals such as: backscattered electrons (BSE), X ray and light. This signals analyse give important morphological informations about analyzed sample. The most important signals are generated by secondary electrons,their number provides this signal intensity creating topographic differences. The emission rate of backscattered electrons is strongly depending by element atomic number Z of analyzed sample. Such SEM equipments could emit characteristic X ray, in this case the intrument is able to give qualitative and quantitative sample informations. This techique advantage over optical microscopy is about area view depth, actually SEM images are apparently three-dimensional.

2.1.2. XDR (X Ray Diffraction)

X Ray Diffraction should give information about crystalline structure of solid sample. This kind of investigations is already used for phase material identifications[2], identifications of elementary cell of crystalline phases determining the dimensions of the crystallite and micro-tensions inside [3], analyzing the peak width. X ray is electromagnetic radiation which has wavelength between 10^{-3}nm -10 nm. They are already used to view inside opaque objects, for instance: medical radiography [4] and computed tomography[5]. This investigation is based on X ray interaction with materials. There are considered strong X ray those which have wavelenght between 0.1-0.2 nm while those that have wavelenght higher are considered weak x-rays. For materials analyze are used strong X ray because their deep penetration inside. Although the materials are considered opaque but in the strong X ray presence these become transparent or translucent. X rays have related wavelenght with atoms dimensions, fact that permits its diffraction by atoms which are arranged in crystalline structures.

X rays diffraction is considered a non distructive method for material internal structures.

2.1.3. Contact angle measurements

Contact angle between a liquid drop and a solid surface is an sensitive indicator of surface energy and chemical structure modifications. Static contact angle between drop water and contact layer gives informations about surface hydrophobicity [6]. If θ angle is lower than 90^o one can say that the liquid wets the solid. If θ angle is higher than 90^o than the liquid does not wet the solid. There is hydrophobic surfaces that have a contact angle higher than 150^o (actually the surface and water drop have not a contact point – Lotus Effect [7].

2.2. Spectral Methods

2.2.1. Inductively Coupled Plasma Optical Emission Spectrometry (ICP-OES)

Normally, this technique is able to analyze more than 70 elements whose concetrations could be lower than 1mg/L. There are a lot of applications of this technique [8]. The ICP-OES spectrometer has the main parts as it is follows: RF generator for plasma initializing, sample introduction which is represented by a peristaltic pump, torch and nebulyzer for sample tranformation into aerosol, instrument optical part which divides the emitted light by wavelenght and a CCD which is a dectection system. To obtain plasma, argon it is used as gas. It is also used to guide the sample through plasma and also for torch cooling. Plasma initializing is working appling a spark for argon inside torch generating electrons extraction from argon atoms. These extracted electrons are accelerated in magnetic coil field. This procedure to bring a suplementary enery for electrons using coil is named inductively coupling. The sample transformed in aerosol by nebulizing process is transported by argon in the central area of plasma. The sample is desolvatated , vaporized , atomized and the analyt species from samples are excited. For being excited, the atoms or ions should pass from the fundamental energetic level to an higher energetic level. The emitted light by the excited atoms arrived in plasma is measured in order to give informations about analyzed sample.

2.2.2. Absorption infrared spectrometry

IR spectrometry has the main applicability for chemical compounds identifying or for structural determinations. This technique is less used for quantitative determinations. The applicability area for this method is large [9-13]. The entire radiation provided by source arrives to a beam splitter where is divided in two beams forming a right angle. One beam is going to a fixe mirror and the other to the mobile one. The both beams are reunited and recombined in the beam splitter and the difference between them generates constructive and destructive interferences (interferograms). The recombined beam arrives to sample and it absorbs the entire characteristic wavelengths for it spectra. The detector records simultaneously the energy variation in time for all wavelengths. There is a modern technique for solid sample investigations based on attenuated reflection named ATR-FTIR. The method is based on radiation passed through a suitable prism at a higher angle then critical one, so that it is developing an evanescent wave on the reflection surface. The interaction of this wave with sample will generate the spectra which than will be recorded.

2.2.3. Molecularly absorption spectrometry in visible and ultraviolet field

This method is based on fundamental law of radiation absorption. For quantitative analysis, the beam is passing through the analyzed sample and it will be measured the transmitted incident radiation intensity. The transmitted radiation intensity will be given by the difference between incident radiation intensity and the intensity of radiation lost due diffusion, reflection and absorption sample constituents. Lambert –Beer law (equation 2.1) realizes the connection between incident radiation I_0, transmitted radiation I and analyzed sample concentration.

$$\log \frac{I_0}{I} = \varepsilon c l = A \quad (2.1)$$

In equation (2.1) the sample thickness is denoted by l and is given in cm, ε means molar coefficient of absorption and is measured in L mol^{-1} cm^{-1}, c represents concentration for analyzed species and is given in moli/L and A is named absorbance. Value of ε is a characteristic for each absorbent species for a specific solvent and wavelenght and is not depending by concentration.

By adding to a UV-VIS spectrometer an integrative sphere equipment it will be able to measure the flat band potential using the diffuse reflection spectra.

2.3. Electrochemical Methods

Electrochemical methods of investigation are clasyfied in two large sections due the nature of used currents so :electrochemical methods using DC and electrochemical methods with alternative current. These techniques are based on process that take places at electrodes when the electrical current pass through the investigate system. In the experimental part of this thesis , there were used as electrochemical methods of investigation the following methods; chronoamperometry at constant potential (maintaining the potential to negative/positive value so that oxidation/reduction process take places), linear sweep voltammetry (meaning to apply electrode a potential with linear variation) and cyclic voltammetry (a variation of potential from anodic zone cathodic zone observing peak corresponding to oxidation/reduction process that take places).

The electrochemical methods of investigation in alternative current used were: electrochemical impedance spectrometry (EIS) and Mott Schottky technique.

Electrochemical impedance spectrometry (EIS) use the record of response signal I(t) when it is appling an alternative current for electrochemical system. The excitation signal is described by equation (2.2).

$$E(t) = E_0 \cos(\omega t) \quad (2.2)$$

E(t) represents the potential at time t, E_0 is the signal amplitude and ω represents angular frequency.

$$I(t) = I_0 \cos(\omega t - \Phi) \quad (2.3)$$

The equation for impedance is:

$$Z = \frac{E(t)}{I(t)} = \frac{E_0 \cos(\omega t)}{I_0 \cos(\omega t - \Phi)} = Z_0 \frac{\cos(\omega t)}{\cos(\omega t - \Phi)} \quad (2.4)$$

The impedance could be represented by plotting like a Nyquist curve or as a Bode diagram (impedance absolute value and phase's angle are plotted *vs* frequency logarithm.

Mott-Schottky technique is used to describe the changes that take places at electrode interface when potential is modified. Frequency remains fixed but it is applying a low excitation signal for potential. Impedance measurements are done to electrode interface when potential varies.

Mott Schottky diagrame are graphic presentation for capacitive and rezistive impedance components plotted as a function of voltage. The rezistive and capacitive components are calculated using equivalent circuits. Mott Schottky proposed an equation for calculating flat band potential :

$$\frac{1}{C^2} = \frac{2}{\varepsilon_r \varepsilon_0 A^2 e N_d}\left(V - F_b - \frac{K_B T}{e}\right) \quad (2.5)$$

C represents capacity, ε_r means dielectric relatively constant, ε_0 is dielectric constant for vaccum, a is electrode surface, N_d represents carrier charges density, V is applied potential, F_b is flat band potential, K_B is Boltzman constant, T is absolute temperature and e reprezents elementary charge.

It is remarkable for this investigation the possibility to calculate charges carrier density for semiconductors from graphic representation of Mott Schottky equation.

Personal contributions

3. Residual titanium flakes as a novel material for retention and recovery of rare earth and relatively rare earth elements

3.1. Introduction

The aim of this study was the valorization of titanium flakes (waste) from titanium and titanium alloy ingot production factories and using in applications related to metals recovery as retention bed for some trace metals. The titanium flakes were anodized for surface nanostructuration with TiO2 nanotubes and then annealed in order to increase the surface stability. The nanostructured titanium flakes were loaded and pressed in a retention column linked with inductively coupled plasma spectrometer (ICP-OES). This system allowed determination of trace elements such as beryllium, lanthanum, lutetium, and ytterbium from sample solutions. Beryllium recovery percentage was over 90%, while lanthanides have just a satisfactory recovery percentage (about 65% Yb and Lu and 50% La). The TiO2 nanotube architecture was not affected during utilization being able to perform for a long time. A thermodynamic and kinetic study was done for beryllium due to its successful adsorption recovery percentage. The obtained results showed that the titanium waste is a promising material for rare earth and relatively rare earth elements retention and recovery.

3.2. Anatas nanotubes preparation

The titanium flakes as received from the production plant were treated in a sonication bath for 15 minutes. The process continues with anodization procedure. The electrolyte was a solution with 0.5% NH4F, 2% distillated water in ethylene glycol. The anodization process was done at 40 V for 2 hours,in an electrolytic cell, using a platinum counter electrode. After anodization, the titanium flakes were annealed for 2hours at 450 °C. This annealing temperature helps nano-architectural TiO2 transforming amorphous structure into crystalline phase [14].

3.3. Column preparation

The crystalline nanostructured titanium flakes were loaded and pressed into a glass manufactured column, 12 cm long with an inner diameter of 0.6 cm. The column was eluted with an acid solution (1% HCl-37% Aldrich) in order to clean and condition it. A glass column was connected online with ICP-OES equipment through a peristaltic pump. Liquid was pushed up through the prepared column into ICP-OES nebulizer.

Three different measurements were performed:

(i) for column regeneration, the acid solution was passed through the column (3 different measurements);

(ii) for synthetic solutionanalysis at pH 12, a solution containing Be, La, Yb, and Lu (5ng/mL each of them) was passed through the column for cation retention (1 measurement); and

(iii) to recover the elements of interest, the acid solution was passed through the column (4 different measurements). Table 3.1 and 3.2.

Working procedure	Type of solution passing through column	Be concentration after passing through column		
		Be ng/ml 234.861 nm	Be ng/ml 313.042 nm	Be ng/ml 313.107 nm
(i) Column regeneration	Acid solution	0.0743	0.1682	0.0698
	Acid solution	0.0610	0.1209	0.0761
	Acid solution	0.0327	0.0910	0.0137
(ii) Cation retention	Be Syntetic Solution 5ng/ml	0.0109	0.0078	0.0376
	Retention percentage (%)	99.78	99.84	99.24
(iii) Elution and cation recover	Acid solution	4.5351	4.5623	4.5631
	Acid solution	0.4410	0.4506	0.3341
	Acid solution	0.2139	0.2138	0.1491
	Acid solution	0.1483	0.1412	0.0480
Recovery percentage after first elution (%)		90.90	91.39	91.95

Table 3.1 Results for Be retention on Ti/TiO2 column

Working procedure	Type of solution passing through column	Lanthanide concentration after passing through column		
		La ng/ml 398.852nm	Lu ng/ml 261.541nm	Yb ng/ml 328.937nm
(i) Column regeneration	Acid solution	0.1765	0.0984	0.1366
	Acid solution	0.9526	0.0196	0.1848
	Acid solution	0.2269	0.0676	0.1335
(ii) Cation retention	Lanthanides synthetic solution 5ng/ml	1.1989	1.4232	1.1738
	Retention percentage (%)	76.02	71.36	76.52
(iii) Elution and cation recover	Elution	2.3675	3.2076	3.2992
	Elution	0.9268	0.2132	0.0340
	Elution	0.4303	0.1472	0.0745
	Elution	0.4813	0.1353	0.0542
Recovery percentage after first elution (%)		62.28	89.68	86.23

Table 3.2 Results for lanthanide retention on Ti/TiO2 column

3.4. Results and discussions

3.4.1. Titanium flakes nanostructuration

Figure 3.1a shows the unmodified waste of titanium flakes aswas collected from titanium ingots production factory. Figure 3.1 b–d presents the SEM images at different magnifications for the nanostructured surface of titanium flakes afteranodization. As it can be noticed in SEM images, at the surface of the titanium flakes, the TiO2 nanotubes are formed. They have a length of about 500–700 nm, and a uniform distribution on the entire surface can be observed in Fig. 3.1 d.

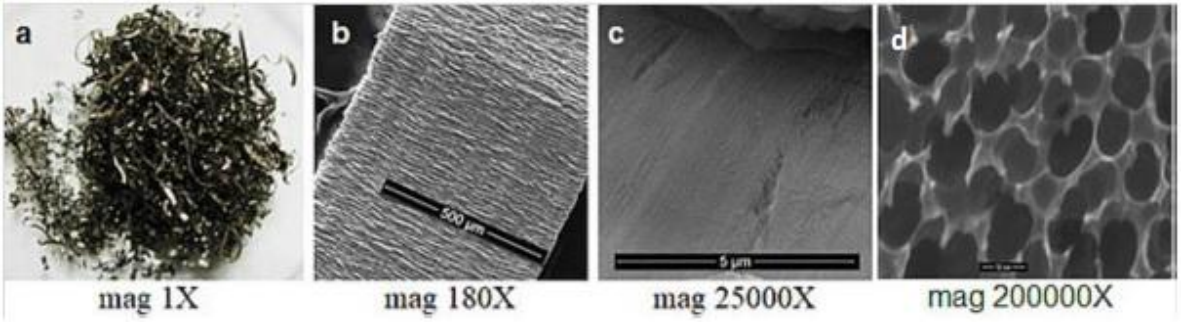

Figure 3.1 (a) optical image and (b–d) SEM images of titanium flakes surface and nanotubes architecture

The X-ray diffraction pattern, presented in Fig. 3.2, clearly indicates the presence of titanium, Ti, (from substrate) and two crystalline forms TiO_2, anatase (A) and rutile (R).

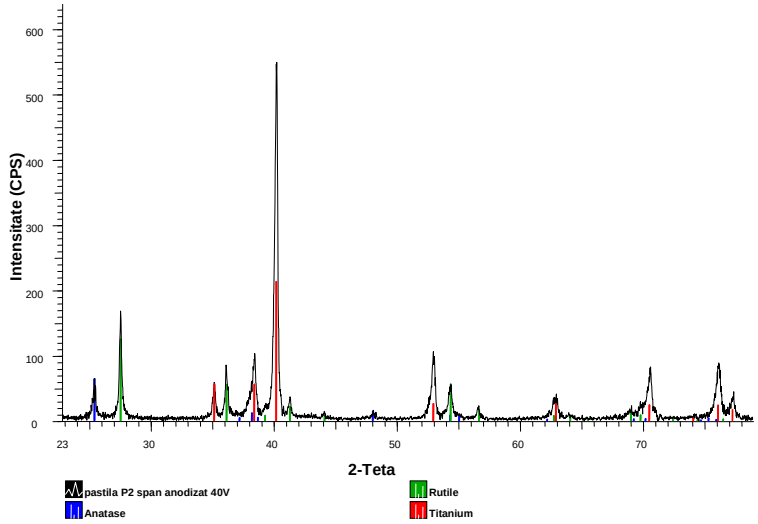

Figure 3.2 XRD patterns obtained of nanostructured Ti flakes after annealing

3.4.2. Beryllium analysis results

According to the working procedure, the Ti/TiO2 column previously used for retention was regenerated and activated with acid solution for a maximum retention of cations. There were selected three different wavelengths for Be to avoid uncertainty about interferences.

The values obtained after column regeneration with acid solution presented in the Table 3.1 show an efficient regeneration after three passing of the solution through column. The Be residual concentrations are insignificant.

In the second step, beryllium is easily retained onto nanotube architecture with the retention percentage over 99%.

Then, in the third step, after elution with acid solution, Be was rapidly and successfully released after the first elution with the recovery percentage of about 91%.

3.4.3. Lanthanide analysis results

Lanthanides have a different behavior than beryllium, and this is the reason we had treated them apart. The retaining percentage of rare earth elements obtained by ICP-OES analysis is presented in Table 3.2.

Rare earth elements like Lu, Yb, and La are not retained totally in column (comparing with

beryllium), but they are recovered partially in the first elution. The retention percentage is presented in Table 3.2, and there are not significant difference values between Lu and Yb. However, the retention percentage for La is lower, 76.02%, suggesting a less efficient retention ability of La on the Ti/TiO2 column. Lu, Yb, and La could be recovered satisfactory by elution (Table 3.2). The retention percentage of Be and of rare earth elements is quite different. An explanation could be their different atomic radius. Be has a smaller volume than rare earth elements, so it can be easily retained inside nanostructure than rare earth elements do. In case of lanthanides, which have a high atomic volume, the nanotubes are either rapidly or partially filled with.

That means that a good part from lanthanide atoms will pass through the column without being retained into nanotubes. This specific behavior of lanthanides is given by adsorption kinetics.

Be adsorption with the best percentage of retention (>99%) and recovery (90–92%) was used for adsorption iso-therms, kinetics and thermodynamics studies.

3.4.4. Beriliu adsorption isotherms

3.4.4.1. Freundlich isotherms

The Freundlich isotherm is one of the most important adsorption isotherm for rough and heterogeneous surfaces with interaction between adsorbed ions and it is descrbed by equation:

$$\mathbf{Q_e = K_F (C_e)^{\frac{1}{n}}} \quad (3.1)$$

Where n is the heterogeneity factor and $\mathbf{K_F}$ is Freundlich constant. For Freundlich model, a good fitting of nonlinear Eq.(3.1) was obtained. The values for n , which is a heterogeneity factor, are higher than 1 (Table 3.3).

Langmuir isotherms				Freundlich isotherms		
Temp(K)	Q_0(L/mmol)	K_L	R^2	K_F(mmol$^{1-1/n}$g^{-1}L$^{1/n}$)	n	R^2
298	1.38x10^{-5}	8993.64	0.9663	7.63x10^{-4}	1.91	0.9667
304	1.16 x10^{-5}	12364.92	0.889	3.70 x10^{-4}	2.25	0.9435
313	1.28 x10^{-5}	13115.01	0.8876	2.11 x10^{-4}	2.72	0.8988
327	1.16 x10^{-5}	20056.31	0.9669	3.14 x10^{-4}	2.74	0.9402
330	1.07 x10^{-5}	25648.03	0.9485	5.69 x10^{-4}	2.08	0.9307

Table3.3 The parametrs for Lamgmuir and Freundlich isotherms

The Be adsorption is indicated by value of n, a chemosorption if n<1 and a favorable physisorption if n>1[15]. The values of n>1obtained in our case indicate that the adsorption of metallic beryllium ions is a favorable physisorption process, probably by the electrostatic interaction of negatively charged deprotonated site to metallic ions.

3.4.4.2. Langmuir isotherms

The Langmuir adsorption model is proposed to describe the monolayer coverage of adsorbate mettalic ions on nanostructurated titanium flake adsorbent site without any interactions between adsorbate ions and adiacente sites. In this isotherm model, all sites are considered equivalent, and the surface is also considered homogeneous [15]. It can be noted that a good fitting of the experimental results was found with this model (see Figure 3.3)

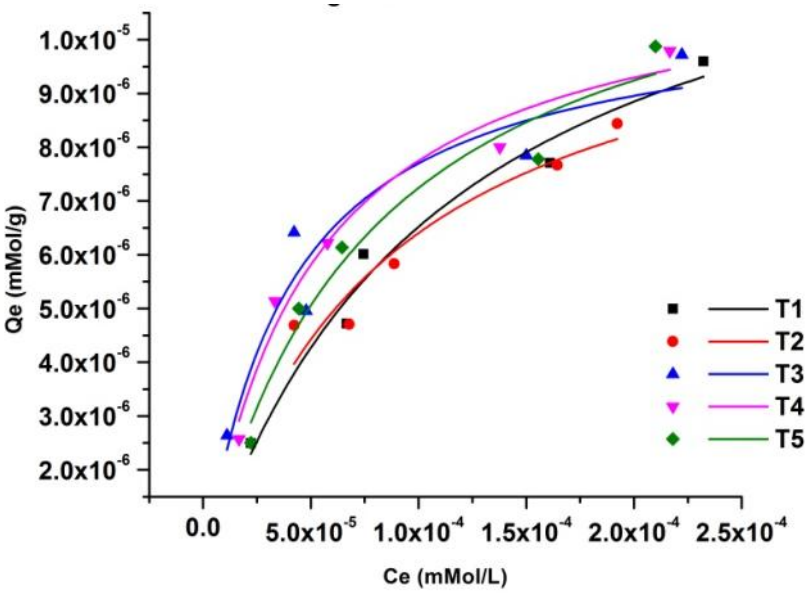

Figure 3.3 Langmuir isotherms

The mathematic equation for Langmuir model is;

$$Q_e = \frac{Q_0 K_L C_e}{1+K_L C_e} \quad (3.2)$$

Where C_e is the equilibrium concentration of Be, Q_e is the adsorption amount in equilibrium state, Q_0 is monolayer adsorption capacity from Langmuir model, and K_L is the Langmuir constant. K_L is a constant which denoted the energy of adsorption and affinity of bindind sites (L/mg) for beryllium ions.

3.4.5. Adsorption thermodinamics

In order to get insight on the adsorption process, the thermodinamic activation parameter of the process were considered. Thus, it can be concluded whether the process is spotaneous or not.Thermodynamic studies including standard enthalpy change (ΔH^o, KJ/mol), standard entropy change (ΔS^o KJ/mol·K) and standard Gibbs free energy (ΔG^o, kJ/mol) were estimated using following Eqs.(3.3 and 3.4).

$$lnK = \frac{\Delta S^0}{R} - \frac{\Delta H^0}{RT} \quad (3.3)$$

$$\Delta G^0 = \Delta H - T\Delta S \quad (3.4)$$

Where K is the equilibrium constant obtained from Langmuir isotherms plots, R is gas constant (8314J/molK), and T is the absolute temperature (K). The linear plotting of lnK *vs*1/T gives the ΔS^o values as intercept and the slope values represent ΔH^o.

Tabel 3.4 presents the calculated ΔG^o values for five tested temperatures and the obtained values of standard enthalpy change and standard entropy change.

ΔGº(KJ/mol)	ΔHº (KJ/mol)	T(K)	ΔSº(KJ/mol·K)
-32.622	23.7	298	0.189
-33.756		304	
-35.457		313	
-38.103		327	
-38.67		330	

Table 3.4 Thermodynamics parameters

The negative values of ΔGº Gibb's energy, which is an adsorption driving force, suggest a spontaneous exothermic process. This is also supported by negative values of enthalpy. ΔGº became more negative at higher temperatures.

The magnitude of ΔHº could give information about the type of sorption. Heat values within 2.1-20.9kJ/mol can be associated with heat evolved during physical adsorption , while the values between 80 and 200 kJ/ mol correspond to the heats of chemisorptions[16] . Therefore, according to the obtained value of ΔHº (Table 3.4) between two ranges, it seems that adsorption of beryllium ions can be associated to a physicochemical adsorption process.

The positive values of ΔSº highlight the affinity of the modified titanium flake surface for beryllium ions. This is also an indication of increased randomness at interface between the solid titanium surface and beryllium solution. The desorbed water molecules gain more translational entropy than lost by Be adsorption, thus generating the randomness in the system. Therefore, we could consider an increase degree of freedom of the adsorbed Be ions.

3.4.6. Be kinetic adsorption

To investigate the adsorption kinetics and adsorption mechanism of Be ions into titanium flake adsorbents, we used three different models to simulate the experimental data: pseudofirst order (PFO), pseudosecond order (PSO) and intraparticle diffusion model (IPD), Figure 3.4.

Nonlinear forms of the PFO model are described in Eq.(3.5)

$$Q_t = Q_e\left(1 - e^{-k_1 t}\right) \text{ (3.5)}$$

Where k_1 is PFO constant rate (1/min), $Q_e$and Q_t(mMol/g) representing the absorbed Be ions number at equilibrium and at time t, respectively. Figure 3.4a shows the fitting of this model on our experimental data with a good coeffient of determination, R2 of 0.993 for 2ng/mL and 4 ng/mL and R2 of 0.996 for 5 ng/mL.

The mathematic nonlinear forms of the PSO model are described in Eq.(3.6);

$$Q_t = \frac{Q_e^2 k_2 t}{1 + k_2 Q_e t_t} \text{ (3.6)}$$

Where k_2 is the constant rate (mMol/g·min).

By plotting t/Q_t vs t at 4 ng/mL Be concentration , a straight line was obtained with a very high coefficient of determination , R2 of 0.995 for 2 ng/mL and 0.999 for 4 and 5 ng/mL.

The Weber's intraparticle diffusion model applied for the adsorption kinetic data analysis is giving information about rate-limiting step in the beryllium adsorption process; whether or not there is an intraparticle diffusion. IPD model is mathematically described by Eq.(3.7).

$$Q_t = k_i t^{0.5} + I \text{ (3.7)}$$

Where k_i is diffusion constant and I is the intercept. By plotting Q_t vs t, a nonlinear dependence with a coefficient of determination, R2 of 0.5 for 2 and 5 ng/mL and 0.81 for 4 ng/mL, was obtained. Thus, the linear dependence for IPD model is far from the linearity coefficient obtained for PFO and PSO. In conclusion, the PSO model gives the best correlation

for beryllium ion adsorption on titanium flakes /TiO2 nanotube surfaces, compared to PFO and IPD model.

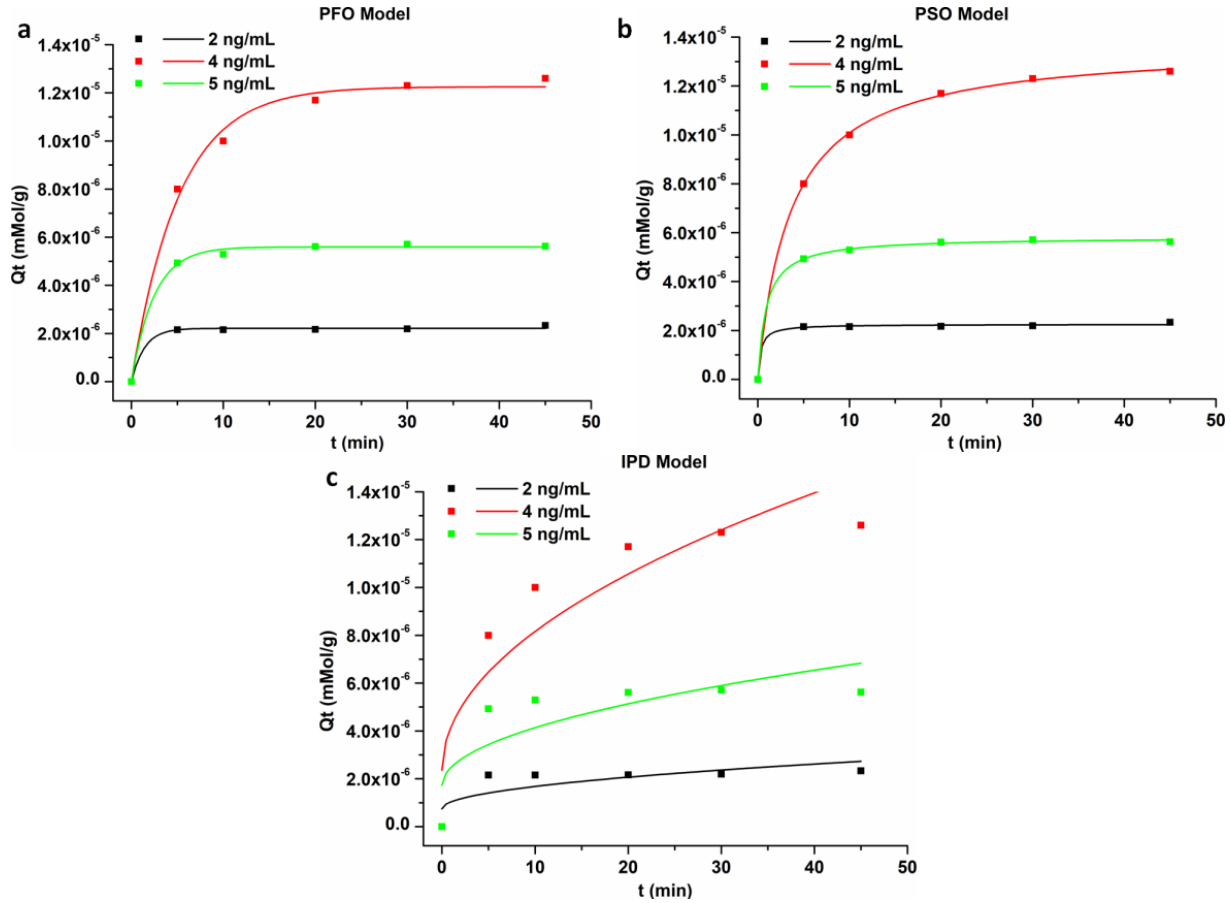

Figure 3.4 Fitting data for tested models (a) PFO model, (b) PSO model, (c) IPD model

3.5. Conclusions

This study presents an efficient way for valorization of titanium flake residue by using applications related to metal recovery as retention bed for some trace metals.

The nanostructure titanium flake surface exhibits retention and releasing properties for rare earthelements La, Lu and Yb and relatively rare earth (Be) elements.

The obtained beryllium recovery percentage of 90% using this waste of titanium is higher than the values reported in literature for more expensive materials.

The column regeneration is facile. The TiO2 nanotube architecture is not affected during utilization , so the column is able to perform for a long time.

From all experimental kinetic studies, Be adsorption on titanium flakes was the best mathematically described by PSO model.

Thermodinamic parametr values suggested a favorable Be adsorption process, spontaneous and endothermic.

Thus, the low-cost titanium flakes (waste resulted from titanium industry), after minimal preparation, could represent a prommising adsorbent material for rare earth and relatively rare earthelement retention and recovery with imediate application in different industrial fields.

4. Titanium industrial residues surface modification towards its reuse as antimicrobial surfaces

4.1. Introduction

Usually, in a titanium factory, there are obtained two important types of titanium such us Ti Gr.2 (Fe, 0.10%; C, 0.02%; N, 0.01%; H, 0.002%; O, 0.13%) and Ti Gr5 (Al, 6%; Fe, max 0.25%; O, max. 0.2%; V, 4%). Ingots scrap have a high content of O and N, around 2000 ppm for O and 200 ppm for N (considering titanium exhibits a high affinity towards these elements) and other alloying elements such as V and Al. These higher O and N amounts represent a problem for conventional recycling processes, so there is a need to find new utilization for this residue.

On the other hand, these impurities are widely presented in scientific literature, having an important role for TiO2 doping providing a significant catalytic activity, generating a better photocatalytic ability of TiO2. N presence in TiO2 semiconductor has a considerable benefit in reducing its band gap, giving the possibility of visible light irradiation absorption instead of UV light as singl TiO2 does [17]. Other investigations showed that TiO2 photocatalytic activity can be also enhanced by V ions doping [18].

Both titania (TiO2) phases (anatase and rutile) were very studied regarding the photocatalytic efficiency and antibacterial abilities. The photocatalytic mechanism involved nanomaterialinteraction with light, generating a photoinduced electron transfer reaction via reactive oxygen species (ROS). The exact antibacterial mechanism of these ROS is not clearly defined; however, it is reported that the hydroxyl radicals (HO•) and superoxide anions (O2•-) resulted under TiO2 irradiation become very reactive with microorganisms. There are many studies that used carotenoids to improve the antioxidant and antimicrobial properties of titanium dioxide coatings [19] [20].

Torularhodin and betacarotene are two compounds in the category of carotenoids and their structures are presented in Figure 4.1.

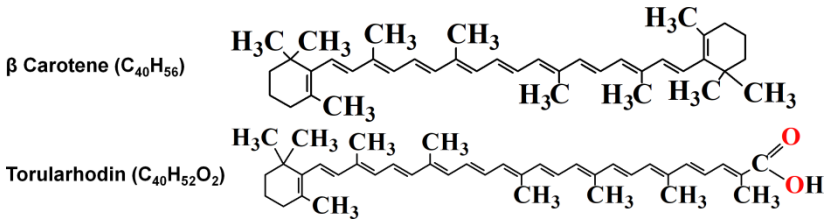

Figure 4.1 Chemical structure for betacarotene and torularhodin

The important difference between their chemical structures is the carboxylic group from the structure of torularhodin. It has polar hydroxyl groups which significantly low the hydrophobic behavior of it offering this molecule the possibility to establish new interaction with TiO2.

TiO2 conduction band, through this binding, may suffer an electron injection from the carotenoid, resulting a carotenoid radical cation formation [21]. β-carotene does not have carboxylic or -OH groups, so its interaction with the hydrophilic oxide surface is expected to be weak.

Subject of this research study was to give a valorization for a residual material provided from a titanium ingots fabrication process. The titanium pressed disk scrap surface was modified with TiO2 nanostructure by a simple and cheap anodization. After nanostructuration, TiO2 nanotube carotenoid (β-carotene or torularhodin) systems were created for an enhanced

antibacterial activity. The new modified titanium scrap surfaces were tested for antibacterial properties against Salmonella typhimurium and Escherichia coli.

4.2. Materials and methods

Titanium scrap (Figur 4.2a) has been cleaned in an ultrasonic bath (ELMA Transonic Ti-H-5) for 15 min using ultrapure water from a Millipore water purification system Direct-Q UV3. The scrap was then dried at 100°C for 1 h long, divided in small portion (amounts of 0.3–0.4g) and pressed in a manufactured hydraulic press. Two hundred-millimeter diameter titanium pressed scrap disks (TiS) were obtained from titanium scrap (Figure 4.2b).

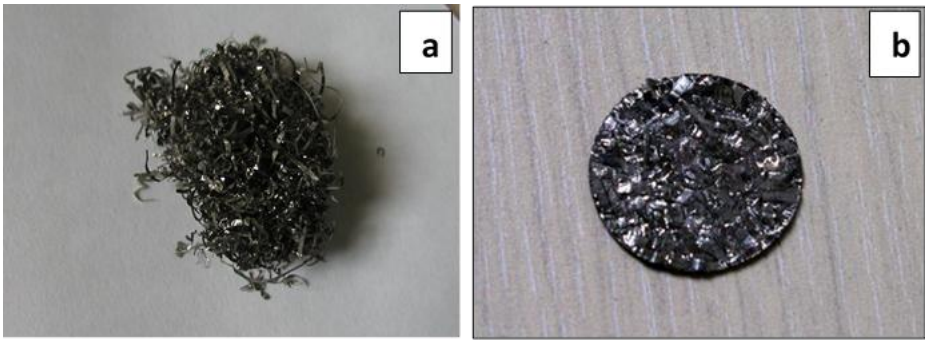

Figure 4.2 Optical images of titanium scrap (a) and TiS (b)

4.2.1. Titanium scrap disks analysis

Nitrogen and oxygen content were determined by analysis of titanium scrap samples with a LECO's TC500-Series having thermal conductivity detector and improved solid-state infrared. Impurities like Al and V were determined using an ICPOES equipment, model 725 (Agilent Technologies).

4.2.2. TiS surface modification with TiO2 nanotubes (TiSTiO2-NT)

The anodization took placed at 40 V for 2h in an electrochemical cell with a Matrix MPS-6005L-2 DC power source. TiS has been fitted as working electrode and a Pt plate served as counter electrode. The organic electrolyte solution was based on ethylene glycol having NH4F 0.5 wt% and ultrapure water 2 v/v %. To improve crystallinity of TiO2 coating, the anodized disk samples were heat treated for 2 h in air, using a LEF-103S-1 furnace (LabTech) set to 450°C.

4.2.3. Torularhodin and beta-carotene deposition

The obtained nanostructure samples, TiS-TiO2-NT, were immersed in solution with 275 μg/L torularhodin for 2 h, in a sterile container. Resulted sample was named TiS-TiO2-NT-T. Other TiS-TiO2-NT samples were immersed in pigment solution containing 375 μg/L β-carotene for 2 h in a sterile container. Obtained sample was named TiS-TiO2-NT-BC.

4.2.4. Samples characterization

Surface characteristics (morphology, topography) of anodized and modified samples were analyzed with a scanning electron microscope (SEM).

XRD analysis were performed at 40 kV and 40 mA on BRUKER D8 ADVANCE (CuKα, λ = 0.154 nm) using DIFFRAC plus XRD Commander (Bruker AXS) software.

UV-VIS investigations were done using a Lambda 950 (PerkinElmer) spectrometer with

sphere sampling module. Recorded absorption spectra led to the construction of Tauc plots followed by optical band gap calculation from linear parts of curves using extrapolation.

The electrochemical surface investigations were performed using an Autolab potentiostat /Galvanostat 302N (Metrohm) with Nova software.

ATR-FTIR spectrum 100 (PerkinElmer) was used for specific functional group determination, having 4 cm-1resolution, between 4000 and 700 cm-1.

4.2.5. Antibacterial assay

Evaluation of antibacterial effect of the tested samples was performed against two pathogenic microbial strains such as Escherichia coli ATCC 8738 and Salmonella typhimurium ATCC 14028.

Antibacterial activity was evaluated by the percentage inhibition of growth, I% [22].

$$I\%=[(B_{18}- B_0)-(C_{18}-C_0)]/ (B_{18}- B_0)\cdot 100 \quad (4.1)$$

where I represents the percentage inhibition of growth, B18 is the compensated optical density at 600 nm, the blank, B0 symbolize blank-compensated OD600 at 0 h, in case of organism positive control, C18 is the organism negative control-compensated OD600 at 18 h, in test sample presence, and C0 is the organism negative control-compensated OD600 at 0 h, in test sample presence. Briefly, sterile samples were placed in a Laboshake Gerhardt shaker for 18 h of incubation at 37°C and 250 rpm. The process took place in 10 mL of Luria Bertani broth sterile medium inoculated with bacteria (1%). Optical density at 600 nm was measured for the samples and control (bacteria culture without sample) to determine the bacterial growth.

4.3. Results and discussions

4.3.1. Titanium flakes nanostructuration

Anodization is one of the most suitable method for growing 1D TiO2 nanotubes regarding ordered alignment and perpendicular dispose to surface substrate. SEM images of anodized titanium pressed disk sample are presented in Figure 4.3: at lower magnification (a) and respectively top view (b) and cross-section images (c, d).

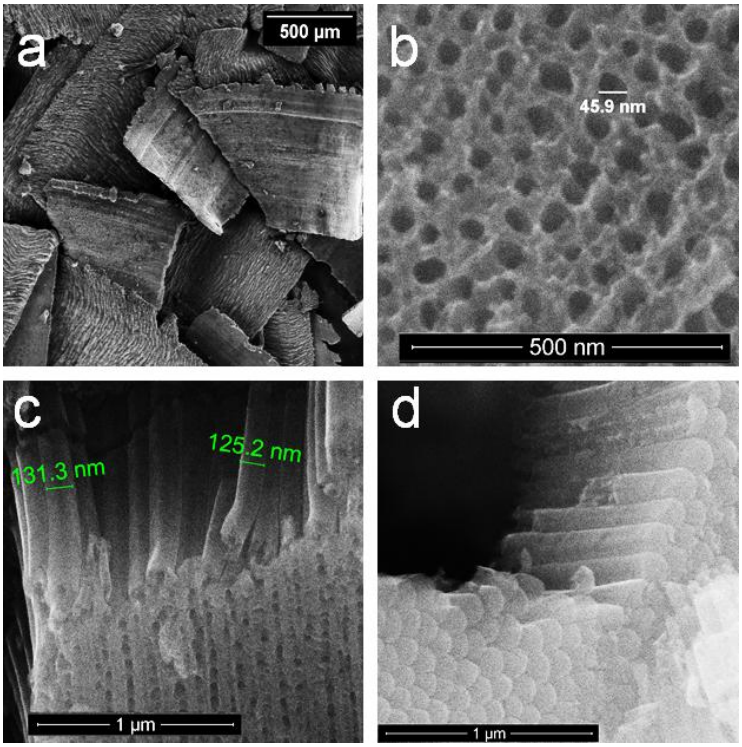

Figure 4.3 SEM images for TiS-TiO2-NT sample: (a),(b) top view, (c),(d) cross-section view

The self-organized TiO2 nanotubes are uniformly distributed on the surface having internal diameters around 45 nm and external diameters around 125–132 nm (Figure 4.3c). Nanotubes are porous on top and closed at bottom. From the cross-sectional images, the nanotubes with a length of around 0.6 microns can be observed. Performance in photocatalytic applications is high in the case of aligned one-dimensional nanotubes because carrier separation is facilitated in these structures. In this way, these features of TiO2 are combined with the advantages conferred by the nanoscale geometry in this TiO2 nanotubular structure in terms of self-ordering, tube length, and diameter. Thus, a superior charge transport takes place in 1D nanostructures over one-dimensional direction.

4.3.2. XRD analysis

The XRD patterns for anodized and annealed titanium disk sample are shown in Fig. 4.4.

XRD patterns exhibited high diffraction peak at $2\theta = 27°$ corresponding to TiO2 R (110) in the rutile phase. Other rutile low peaks can be observed at 36°, 41.25°, 54.20°, and 56.51°. At 2θ value of 25.3°, peak corresponding to A(101) anatase can be found as a major peak.

3.02 eV is band gap energy for rutile TiO2, being smaller compared to the one for anatase which is 3.23 eV. Between these two crystalline forms, rutile is more stable, while anatase has superior photocatalytic properties [23]. Either rutile or anatase crystalline phases presence in different percentage was studied in order to improved photocatalytic efficiency for materials. A composite of anatase and rutile where the electron transfer can occur between the two such phases has been found to display highest photocatalytic efficiency causing an increase in charge separation and a lengthening in electron-hole pair lifetime.

TiO2 anatase (wA) and rutile (wR) phase weight percentage from the TiS-TiO2-NT samples total crystalline phase were quantitatively estimated using Eqs.4.2 and 4.3 shown below [24].

$$\% w_A=[1/(1+1{,}26 \text{ X } I_r/I_a)] \times 100 \quad (4.2)$$

$$\% w_R=[1/(1+0.0884 \times Ia/Ir)] \times 100 \quad (4.3)$$

where signal intensities Ir and Ia are determined from the XRD plots assigned to rutile R(110) and anatase A(101). 0.884 and respectively 1.26 from these equations represent scattering coefficients. Weight percentages for the two phases, anatase and rutile, were 32.25 wt% for the first and 66.75 wt% for the second one.

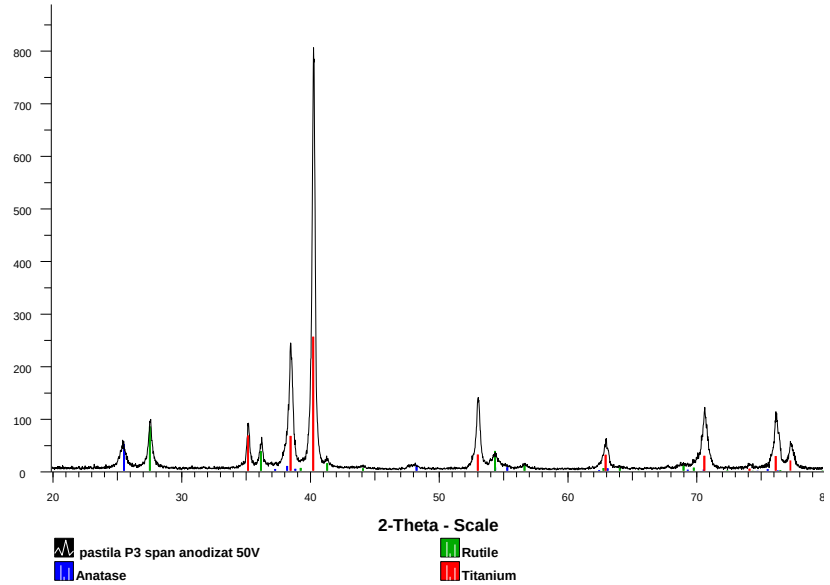

Figure 4.4 The XRD patterns for anodized and annealed Ti flakes (*TiS-TiO_2NT)*

4.3.3. TiS-TiO2-NT surface modification by torularhodin and β-carotene deposition

After anodization and annealing procedure, the nanostructured titanium flake surface was modified by immersion in β-carotene and torularhodin solutions.

4.3.4. FT-IR analysis

FT-IR recorded for anodized sample in Figure 4.5a showing the broad peak in region between 3100 and 3400 cm-1 can be due to stretching vibrations caused by OH groups on the surface [19]. Other peaks evidenced are the one at 1380 cm-1 (assigned to Ti-O) and the one around 1640 cm-1 (corresponding to bending modes of Ti-OH [25] or vibrations of coordinated H2O. Ti-O-Ti bonds presence can be seen by peak appearance at 1160 cm-1 [26] . The peak at 904 cm-1 can be associated with a four-coordinate Ti–O stretching vibration [27]. Ti-O stretching modes (in which nonbridging oxygen atoms are involved) can be evidenced by the peak at 890 cm-1 [28].

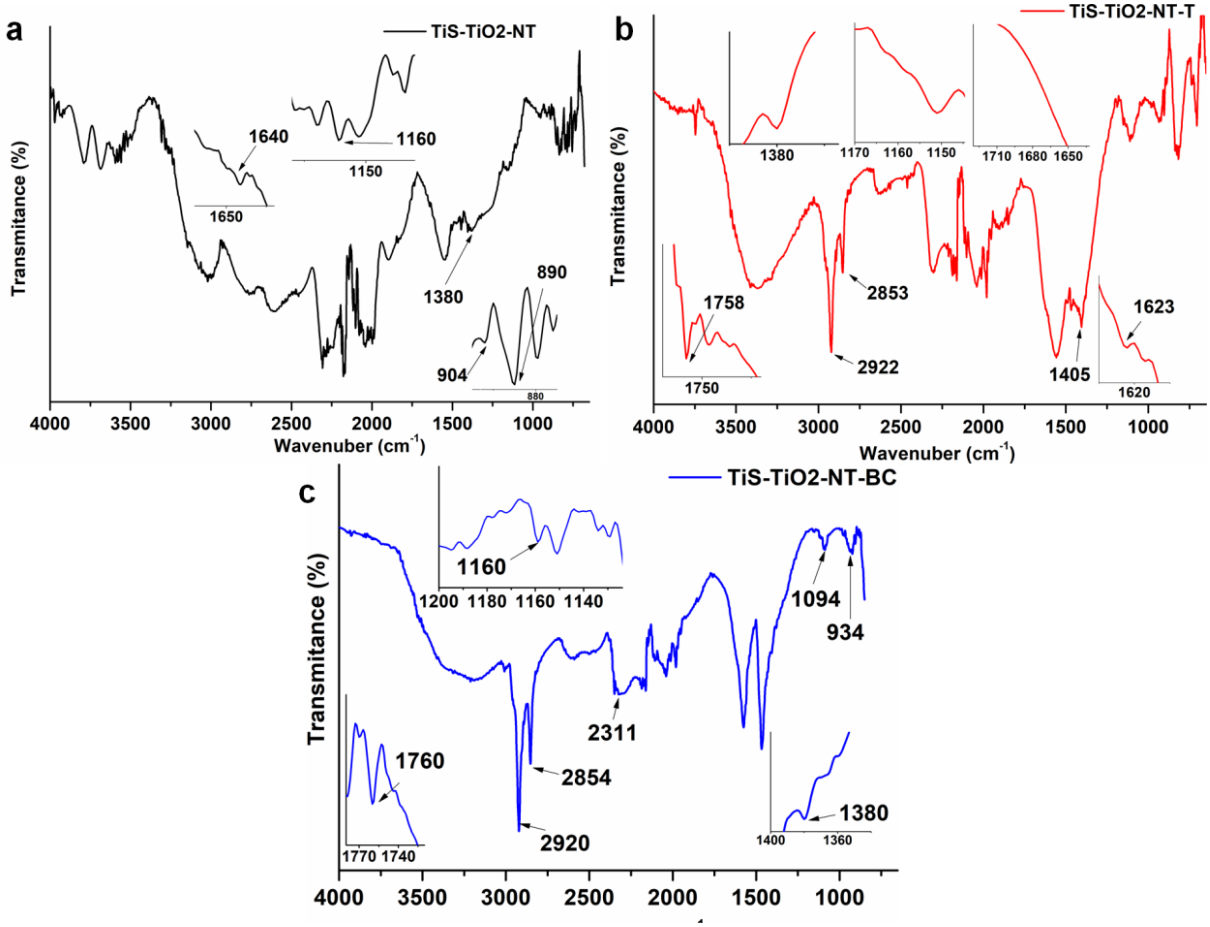

Figure 4.5 FT-IR spectra corresponding to modified Ti scraps: (a) TiS-TiO2-NT, (b) TiSTiO2-NT-BC, and (c) TiS-TiO2-NT-T.

Spectra corresponding to TiS-TiO2-NT-T (Figure 4.5b) present peaks at higher wavenumbers: at around 3400 cm-1 peak assigned to -OH group stretching and aliphatic CH3 and CH2 groups show asymmetrical and symmetric stretching vibrations peaks at 2922 cm-1 and at 2853 cm-1[19, 29] . In the middle area of the spectrum, peak corresponding to a free carboxyl group stretchingis visible in inset: the peak at around 1700 cm-1 for C=O. The peak at 1623 cm-1 (seen in inset) can be attributed to Ti-OH. This peak was also present in the case of TiO2 sample at 1640cm-1. The peak at around 1380 cm-1 assigned to Ti-O is present, but its intensity decreased compared to TiS-TiO2-NT. The peak at 1160 cm-1 assigned to Ti-O-Ti bond is not visible anymore. The peak at 1680 cm-1 assigned to a stretching vibration of a carboxylic acid is not present, instead a sharp peak at 1405 cm-1 for carboxylate anion (COO-) symmetric stretching is present [30]. These could suggest a chemically bound between torularhodin and TiO2 nanotubes rather than simply adsorption, as literature mentioned.

In the FTIR spectra of TiS-TiO2-NT-BC sample (Figure 4.5c), at around 3400 cm-1, a broad peak can be seen, showing also the presence of hydroxyl group stretching [31]. -CH2- asymmetry and symmetry stretching is indicated by the two sharp peaks, close to each other, seen at 2920 cm-1 and 2854 cm-1 [31]. Peak from 1760 cm-1 can prove carbonyl groups presence byC=0 stretching [32]. The peak at 2311 cm-1 marks the presence of conjugated phenol [33]

The specific areas of trans =CH present in β-carotene were identified by the peak assigned to thedeformation mode of trans-conjugate alkenes, visible at 934 cm-1. [34]

Ti-O bond at around 1380 cm-1 and Ti-O-Ti at 1160 cm-1 are still visible at this sample. From all these, we can conclude that β-carotene is adsorbed on TiO2, in good agreement with literature.

4.3.5. Contact angle measurements

The wettability of TiS and modified samples, TiS-TiO2-NT, TiS-TiO2-NT-T, and TiS-TiO2-NT-BC, was established by contact angle measurements. For TiS a hydrophilic character was observed. The obtained average value was 81° ± 2.05, close to 90°. TiS-TiO2-NT was showing hydrophilic nature, the obtained value being 64° ± 1.5. It is more hydrophilic compared to TiS. Adding carotenoids to the surface made the surface more pronounced hydrophilic. TiS-TiO2-NT-T was presenting an average value of 22° ± 1.8. For TiS-TiO2-NT-BC, the obtained value, 37° ± 1.2, was a little higher compared to the one for TiS-TiO2-NT-T.

4.3.6. Optical energy gap determination

The band gap energy was estimated according to literature The band gap energy was estimated according to literature considering the absorption spectra as a spectral contribution of two components: a semiconductor (TiO2 nanotube surface) modified with an organic compound (β-carotene/torularhodin). It used the fundamental peak linear fit from Tauc plot. Additionally, the points which can be found lower than the fundamental absorption were linear fitted, and the slope was used as an abscissa. The band gap energy was estimated from the two fitting line intersections, as shown in Figure 4.6

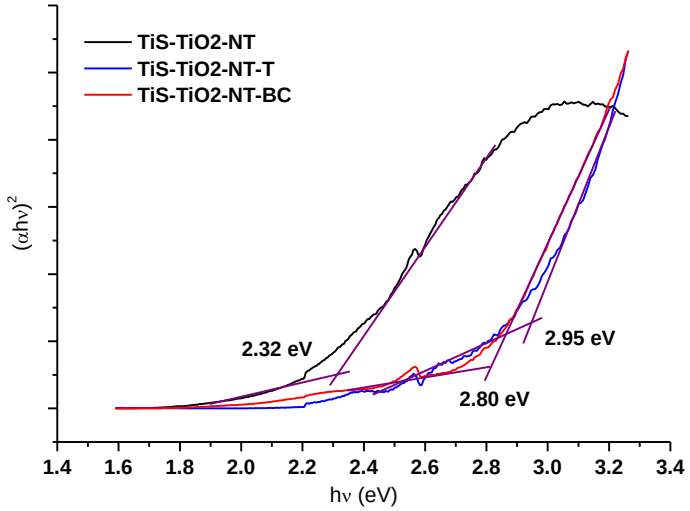

Figure 4.6 Dependence of (ahν)2 of modified and unmodified TiSTiO2-NT samples upon the incident photon energy (hν)

The drawback of wide band gap of 1D TiO2 was usually defeated by doping. In our case, the narrow band gap was sustained by increased N and O containing 200–300 ppm for N and up to 2000 ppm for O due to mechanical titanium ingots processing and Al and V amount (5.56±0.16% Al and 3.68 ±0.12% V) which are normally alloyed elements required by titanium ingots standard fabrication. All these elements play the role of dopants, hindering photogenerated electrons/hole pair recombination and allowing absorption of light into the visible range.

Band gap energy measurements revealed for pure TiO2 rutile phase a value of 3.0 eV and 3.2 eV for pure TiO2 anatase phase. Compared to these, the obtained energy band gap value of 2.32 eV for TiS-TiO2-NT unmodified is lower. A diminished band gap energy could be associated with an energy level change within TiO2 band gap caused by a dopant presence. Nitrogen being present at the TiO2 surface is also known to narrow the band gap, according to literature [35].

The presence of carotenoids on titanium disk scrap surfaces leads to the widening of the band gap at 2.8 eV for TiS-TiO2-NT-BC sample and 2.95 eV for TiS-TiO2-NT-T sample.

4.3.7. EIS analysis

Obtained EIS results (Nyquist and Bode modulus plots) for modified Ti scrap, TiS-TiO2-NT, TiS-TiO2-NT-T, and TiSTiO2-NT-BC, are shown in Figure 4.7 a and b. Data were fitted using the equivalent circuits shown in Figure 4.8. For TiSTiO2-NT sample, a TiS coated with a nanotube porous layer, the electrical circuit from Figure 4.8a was proposed. Rs is electrolyte (aqueous NaCl 0.9%) resistance. The CPENT (constant phase element) placed in parallel with resistance RNT correspond to the nanotubes layer. Barrier oxide layer is represented by CPEBO placed in parallel with RBO. For the two samples with carotenoids, TiS-TiO2-NT-T and TiS-TiO2-NT-BC, circuit from Figure 4.8b was used, having additional elements: Rcar in parallel with CPEcar added for the deposited carotenoid layer. CPE has two components, N and Y0, where N (having values between 0 and 1) is an empirical constant and Y0 is 1/ |Z| - admittance value when ω is 1 rad/s. Parameters for corresponding proposed circuits are listed in Table 4.1. Resistance attributed to barrier oxide layer (RBO) has very closed values, in the same magnitude order (around 25 kohms), for all samples. Resistance associated to nanotubes layer (RNT) is higher for carotenoids modified samples compared to unmodified one. For TiS-TiO2-NT-BC sample, this resistance became significantly higher (up to 686 Ω) compared to the one for unmodified TiS-TiO2-NT sample (60Ω). However, for TiS-TiO2-NT-T the RNT value (85 Ω) is only a little higher compared with unmodified sample. The difference between the two carotenoids is visible also in Rcar value. It is about five times higher for TiS-TiO2-NT-BC compared to TiS-TiO2-NT-T. All these higher resistance results should be an indication of corrosion and photocorrosion resistance and an increased stability for all tested samples. N values of CPEBO for barrier oxide layer indicate a pseudo-capacitive behavior for all samples. For CPENT and CPEcar corresponding to NT and carotenoids layers, values for N are around 0.5, indicating a diffusion mechanism through these layers.

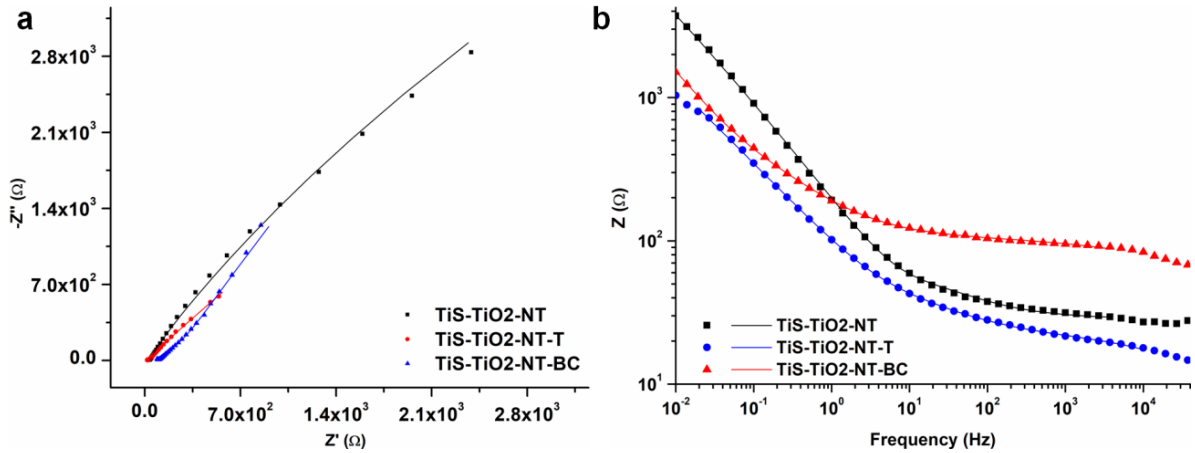

Figure 4.7 EIS analysis for TiS-TiO2-NT, TiS-TiO2-NT-T, and TiSTiO2-NT-BC: (a) Nyquist diagram, (b) Bode modulus diagram

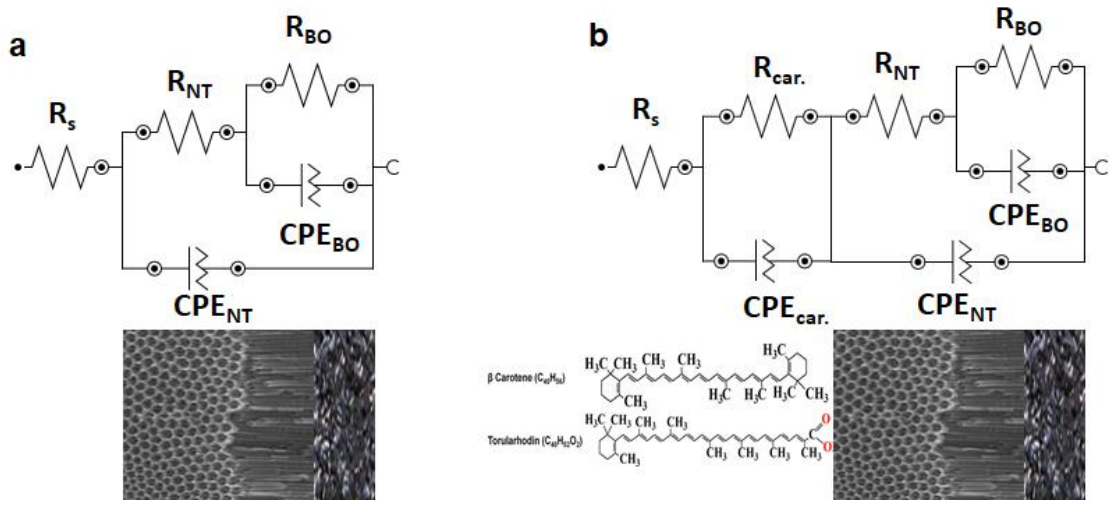

Figure 4.8 Proposed equivalent electrical circuits used in EIS data fitting of (a) TiS-TiO2-NT and (b) TiS-TiO2-NT-T; TiS-TiO2-NT-BC

Parametri / Probă	R_s [Ω]	$R_{car.}$ [Ω]	$CPE_{car.}$ N	$CPE_{car.}$ Y_0 [$S \cdot s^n$]	R_{NT} [Ω]	CPE_{NT} N	CPE_{NT} Y_0 [$S \cdot s^n$]	R_{BO} [Ω]	CPE_{BO} N	CPE_{BO} Y_0 [$S \cdot s^n$]	χ^2
TiS-TiO2-NT	28.5	-	-	-	60.52	0.6	$1.3 \cdot 10^{-3}$	$27.9 \cdot 10^{3}$	0.97	$0.3 \cdot 10^{-3}$	0.17
TiS-TiO2-NT-T	3.10	18.2	0.57	$3.4 \cdot 10^{-3}$	85	0.5	$3.4 \cdot 10^{-3}$	$24.8 \cdot 10^{3}$	0.82	$0.6 \cdot 10^{-3}$	0.01
TiS-TiO2-NT-BC	15.7	89.3	0.45	$0.3 \cdot 10^{-3}$	686.18	0.65	$2.5 \cdot 10^{-3}$	$28.4 \cdot 10^{3}$	0.81	$2.4 \cdot 10^{-3}$	0.01

Table 4.1 Parameters for fitted circuits corresponding to modified scrap samples

4.3.8. Mott-Schottky analysis

Efb values, which are dependent on the recombination process and interface charge transfer[36] were estimated from Mott Schottky diagram for TiS-TiO2-NT modified and unmodified sample Figure 4.9. For a photo-electrocatalytic process, it is desired to have a large and negative Efb [36].

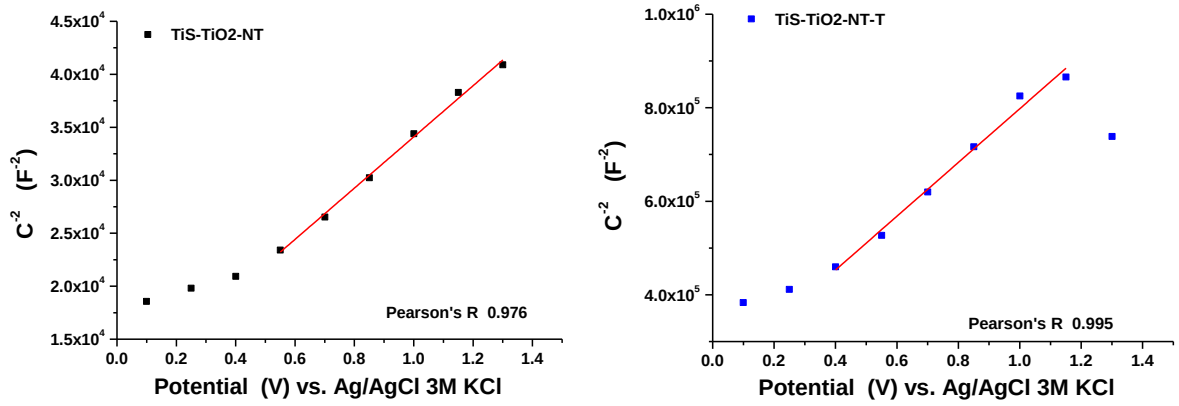

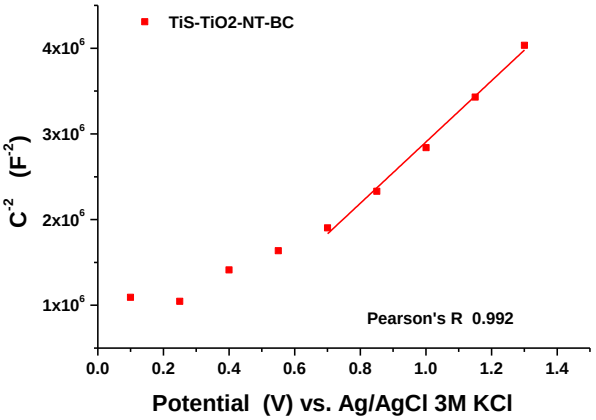

Figure 4.9 Mott Schottky plotting at 1000Hz

The calculated value of Efb for unmodified TiS-TiO2-NT is -0.305V. For modified surfaces, Efb is shifted to a more negative value after torularhodin deposition (-0.388V) and on the contrary towards the more positive value (0.187 V) after β-carotene deposition. Thus, it should be pointed that from the Efb point of view, the TiS-TiO2-NT surface modification with torularhodin improves the photo-electrocatalytic abilities of the surface.

4.3.9. Cyclic voltammetry

CV curves for modified TiS samples are presented in the Figure 4.10. It can be observed that the inner area of the CV curve decreases after surface modification suggesting a reduction of the capacitive behavior due to the higher electrical resistance of the carotenoid coatings. From the CV plots, samples double-layer capacitance (Cdl) was determined as the ratio between I (the average current density recorded during the potential sweep from 0.5 V to 1 V to the anodic direction) and the scan rate (Eq.4.4).

$$C_{dl} = I/s \quad (4.4)$$

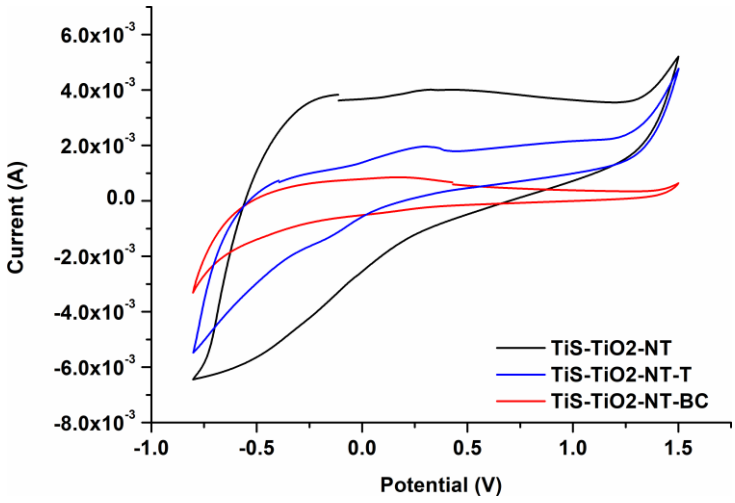

Figure 4.10 CV plots of modified and unmodified TiO2 nanotube scrap surfaces

For TiS-TiO2-NT, Cdl = 98.28 mF/cm2, Cdl corresponding to TiS-TiO2-NT-BC is 15.47mF/cm2 and the one for TiS-TiO2-NT-T is 48.025 mF/cm2.

4.3.10. Antibacterial activity

Antibacterial activity is presented in Figure 4.11 for TiS-TiO2-NT modified and unmodified sample using Salmonella typhimurium and Escherichia coli as bacteria.

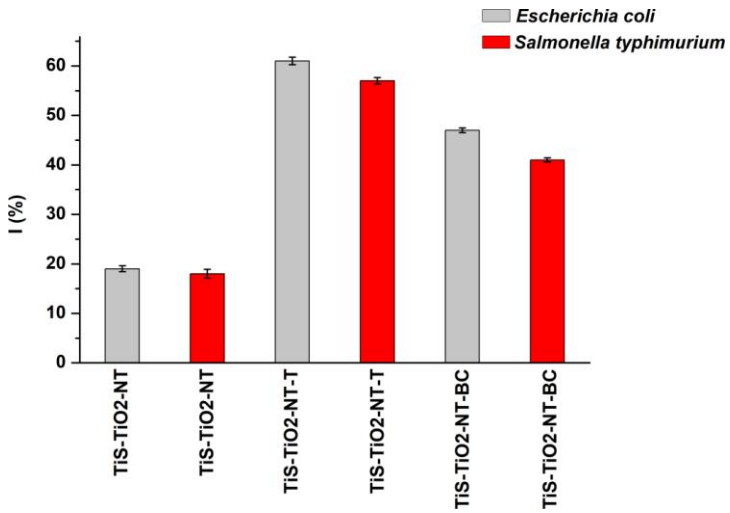

Figure 4.11 Antibacterial activity for the modified titanium flake surface

The action mode of photoactivated TiO2 against microorganisms has been studied by many authors.The killing action was proposed by Matsunaga et al. to be by depletion of coenzyme by dimerization and subsequent inhibition of respiration [37, 38] and the antibacterial action is due to membrane and cell wall damage (see SEM image below).For the samples containing carotenoids, a higher antibacterial effect can be observed. The highest degree of inhibition is represented by samples containing torularhodin. Figure 4.12 shows the SEM images of Salmonella typhimurium on the titanium substrate before and after surface treatments.

On the TiS sample, a field of Salmonella bacterium was observed with a phenomenon of membrane bulging. Membrane bulging is indicated in Figure 4.12a, inset; an explanation for membrane bulging formation would be the more pronounced roughness and the need of microorganisms to form compact structures to stay attached to the scrap surface. When the sample is treated (Figure 4.12b), in this case by anodizing, the microorganisms form larger networks to adhere better to the surface of the scrap. The cells that form the cluster are numerous compared to the sample which contains beta-carotene or torularhodin (Figure 4.12c–d). Figure 4.12 d1 shows a small chain of cells (Salmonella bacterium), but these are modified toward typical bacterium cells. Severe damages can be observed on the cell wall (Figure 4.12d2).

The cell damage can be due to the torularhodin role cumulated with the antibacterial effect of titanium nanotubes [19].

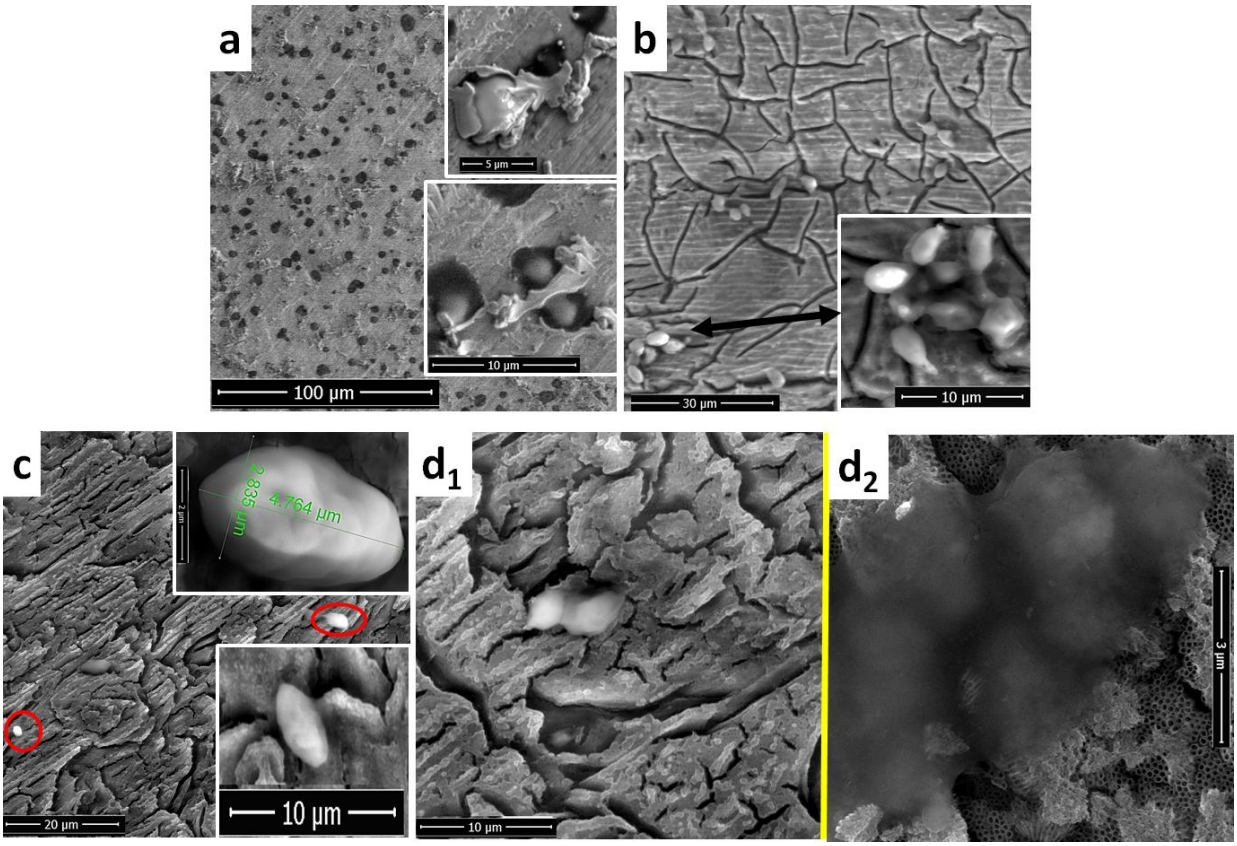

Figure 4.12 SEM images of *Salmonella typhimurium* attached onto the Ti with different treatment conditions: (a) Ti scrap; (b) TiS-TiO2-NT; (c) TiS-TiO2-NT-BC; (d1, d2) TiS-TiO2-NT-T

Figure 4.13 presents SEM images of Escherichia coli attached onto the TiS modified and unmodified samples. On the titanium scrap samples, many intact and independent Escherichia coli cells can be seen, having their typical morphology (Figure 4.13a). In the case of the anodized scrap, aggregation/clumping of bacterial cells can be observed, cells being closely related to each other (Figure 4.13b). Figure 4.13c indicates inter-cellular bond connecting neighboring cells (cell clustering) where beta-carotene was added. Flattening and deformation of E. coli cells is observed on anodized scrap with torularhodin (Figure 4.13d). There is a major decrease of microorganism's number when using the two carotenoids: torularhodin and β-carotene to coat the nanostructured sample.

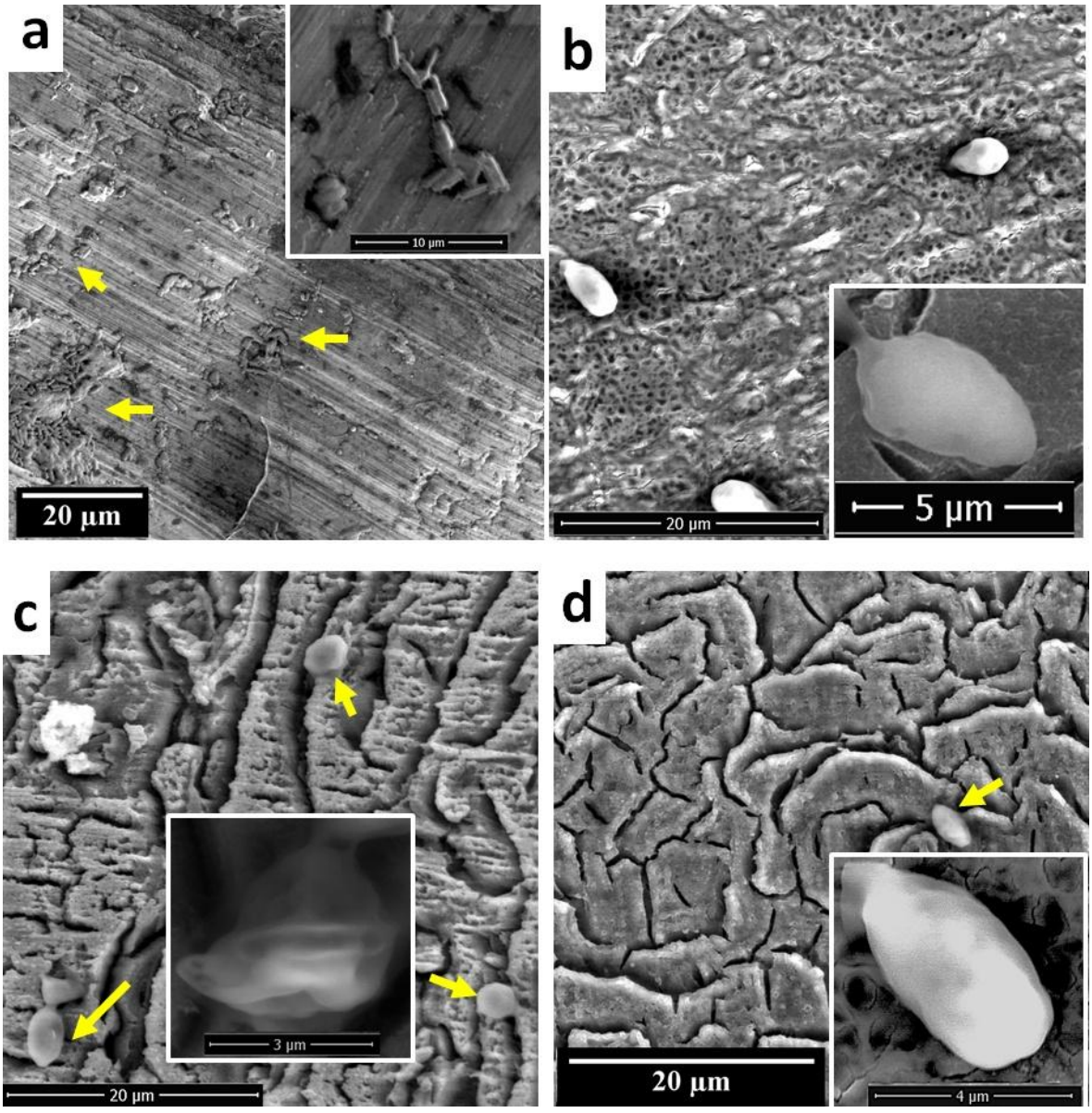

Figure 4.13 SEM images of Escherichia coli attached onto the Ti with different treatment conditions: (a) scrap, (b) TiSTiO2-NT, (c) TiS-TiO2-NT-BC and (d) TiS-TiO2-NT-T

4.4. Conclusions

Started from a waste material provided from titanium industry ingots fabrication process, we generated, after a few simple and inexpensive treatments, a new material with antibacterial behavior. V, Al, and N impurities which turned titanium into a residue prove beneficial for electrochemical and semiconductor properties of titanium scrap. To increase antibacterial properties, the TiS surface was nanostructured and then modified with two different carotenoids: torularhodin and β-carotene. Structural differences between the two carotenoids were reflected in the surface properties and antibacterial activity. The bactericidal treatments were performed against two Gram-negative bacteria, Escherichia coli and Salmonella typhimurium, showing a percentage of growth inhibition around 60% against both tested bacteria, suggesting their suitability to efficiently reuse as an antibacterial material.

5. Nanostructured TIO_2/TI based electrodes obtained from titanium scrap

5.1. Introduction

Another application for titanium scrap presents in this thesis it is about TiO2/Ti electrode obtained used for phenol degradation. The new electrode was created using anodization in order to create a TiO2 nanostructurate architecture on its surface. TiO2 is able to create huge active surfaces capabile to retain inside different metallic ions improvenig its photicatalitic properties.

TiO2 has three christallyne phases : anatase, routile and brookite. Anatase has the strongly photocatalytic activity [39]. Anatase copper doping was used in this experimental in order to improve photocatalytic behaviour narrowing band gap from (3.2 -3.4 eV) to (1,6eV) [40].

This new created electrode is used for phenol degradation. Phenol degradation is based on photocatalytic effect generated by TiO2 copper doping that is responsible for generating electrons –holes pairs. In the light condition, these generated pairs are responsible for hydroxil radical obtaining that probabily attac the aromatic nucleus oxidizing it till finally oxidation compounds (CO2 and H2O) are formed.

5.2. Materials and Methods

5.2.1. Ti scrap anodization

Small pieces of titanium scrap provided from titanium ingots processing, having 1mm thickness and 20 mm long were modified by anodization in order to obtain a TiO2 nanostructured surface. The scrap was first cleaned in purified water in an ultrasonic bath for 15 minutes. After that, it was immersed in a solution of HF and HNO3 for 5 seconds. Freshly obtained samples were fixed in the electrochemical cell as an anodic electrode using a Pt foil as counter electrode. A MATRIX MPS-7163 as electrochemical source was connected to the electrochemical cell. TiO2 nanostructure was achieved applying a raising voltage from 0 to 40 V, with 2 V /10 s step and then kept it constant 2 h at 40V, at room temperature [41]. We used as electrolyte solution ethylene glycol with 0.5% NH4F and 2% purified water. After anodization, the obtained samples were rinsed with distilled water. At the end, samples were annealed at 450° C for 2 h for a better sample crystallinity.

5.2.2. Copper doping

Copper doping was realized into a three electrodes electrochemical cell, using anodized and annealed Ti scrap as working electrode, a Pt (Metrohm) counter electrode and Ag/AgCl, 3 M KCl, (Metrohm) as reference electrode. Electrodes were immersed in 1mM $CuSO_4$ solution. SO_4^{2-} anions concentrationhas been set to 10^{-1} M with H_2SO_4 solution to ensure a high conductivity during the reduction process and the pH was adjusted to 3 with NaOH solution. Copper doping was realized by applying reduction potential pulses of -0.4V related to OCP (Opened Circuit Potential) on the working electrode (60 reduction potential pulses of 200ms) [42]. The reduction potential of -0.4V has been chosen after a single cyclic voltammogram (sweep rate =20mV/s). During the reduction sweep to a negative potential, an increase in the cathode current begins at -0.3V with a visible maximum around -0.4V which can be associated with the reduction of Cu^{2+} ions to metallic Cu on the titanium scrap NTs surface. During the pulsed electrode deposition process a first pulse of -1.0V is applying during 200ms. Then a 60 repetitive sequence of modulated potential is applied. A reduction potential of -0.4V is applied during 200ms immediately followed by a +0.05V pulse (stripping potential) of 50ms. The first pulse was applied to induced nucleation of Cu nanoparticles into scrap NTs surface. The

stripping potential was used to fix Cu nanoparticle size while -0.4V potential was used to slowly growing Cu nanoparticles (Figure 5.3).

5.2.3. ICP-OES investigation

To prove Cu containing in titanium scrap sample (after electrochemical Cu doping and all electrochemical tests were done) it was used ICP-OES Agilent Technologies 725 equipment.

5.2.4. XRD analyses

DRX analyses were performed on BRUKER D8 ADVANCE using DIFFRACplus XRD Commender (Bruker AXS) software to detect TiO2 polymorphs phases.

5.2.5. Phenol degradation

The modified electrodes were used for phenol degradation. Experiments were carried out using the same Autolab 302N and the same three electrodes cell. The measurements were performed in the potential range: 0 – 1.4V, with a 2.4mV step and 10mV/s scan rate. Electrolyte solution was 10 mM phenol in Na_2SO_4 0.5M. Eight LSV repetitive measurements were performed to describe the transformation that took place.

5.3. Results and discussion.

5.3.1. Surface modification

Figure 5.1 illustrates the recorded current versus time curve during titanium scrap anodization procedure. As it is shown in Figure 5.1, the curve has three distinctive areas. The first one corresponds to a strong titanium scrap oxidation phenomenon and as a result, a compact oxide layer is formed on the scrap surface. The red marked area corresponds to the formation of pits in oxide layer while the last one area corresponds to the generation of TiO2 nanotubes on titanium scrap. The charge obtained integrating the area under current time curve was 18.83 C.

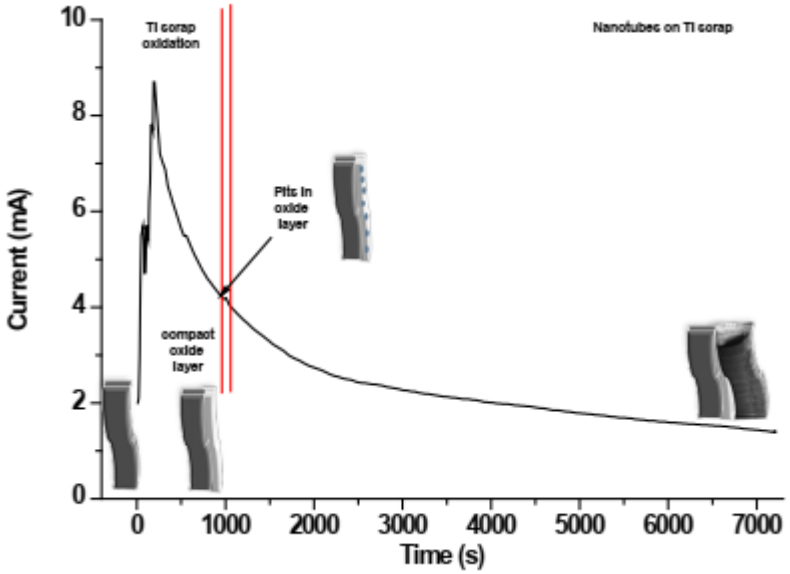

Figure 5.1 Record current *vs* time for titanium scrap anodization

5.3.2. SEM images for anodized titanium scrap

SEM images with various magnifications presented in Figure 5.2a-d, clearly shows a large

area of TiO2 nanotubes formed on anodized titanium scrap.

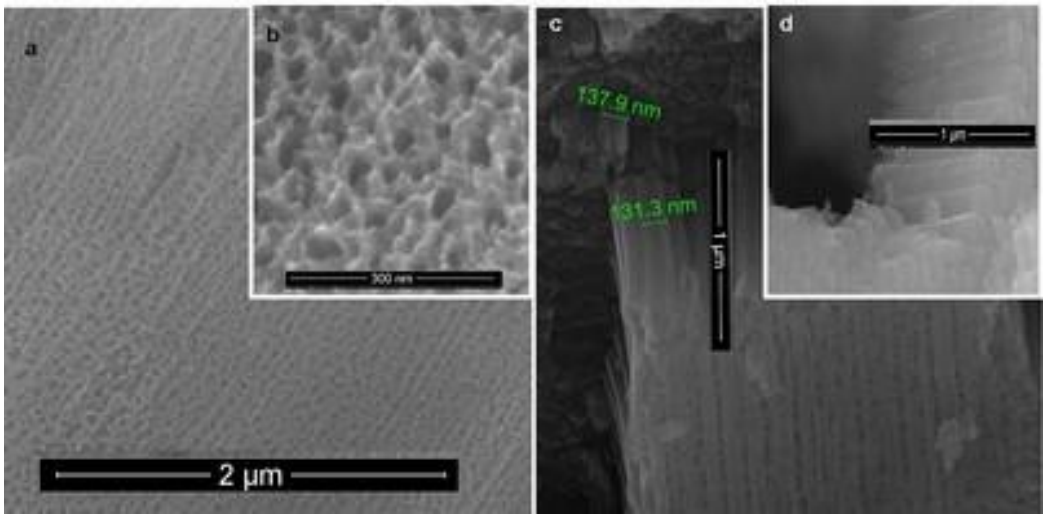

Figure 5.2 SEM images for annealed and anodized titanium scrap samples at different magnifications: a,b- top view of nanotubes, c- images of nanotubes (for diameter and high dimension details), dimage of nanotube presenting cap end

5.3.3. Copper doping

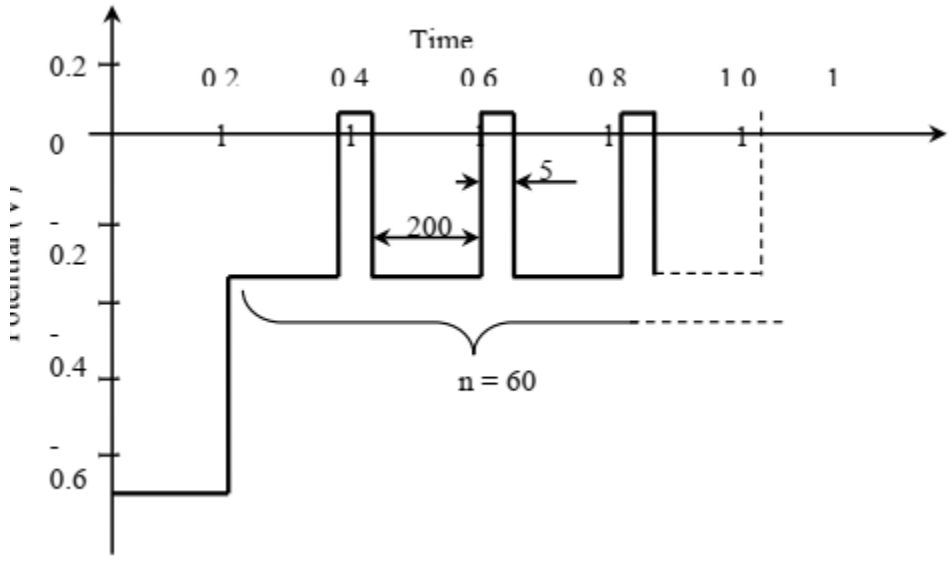

Figure 5.3 Schematic representation of modulation potential applied for copper deposition

Figure 5.3 represents the potential modulation used for copper deposition . The first pulse at 1V potential induces nucleation of Cu nanoparticles (CuNPs) onto titanium scrap NT surface.

The positive potential of +0.05V was used to fix the CuNPs size while the potential of -0.4V was used to slowly grow CuNPs resulting in this way rich Cu deposit. The modulation potential consist in a 60 repetitive sequences of 15 seconds between -0.4V (the deposition potential) and +0.05V.

The SEM images presented in Figure 5.4 correspond to TiNTsCuNPs samples obtained. The light area observed in SEM images presented in Figure 5.4 a-b is due to the copper nanoparticles. Copper presence was proved by ICP-OES technique.

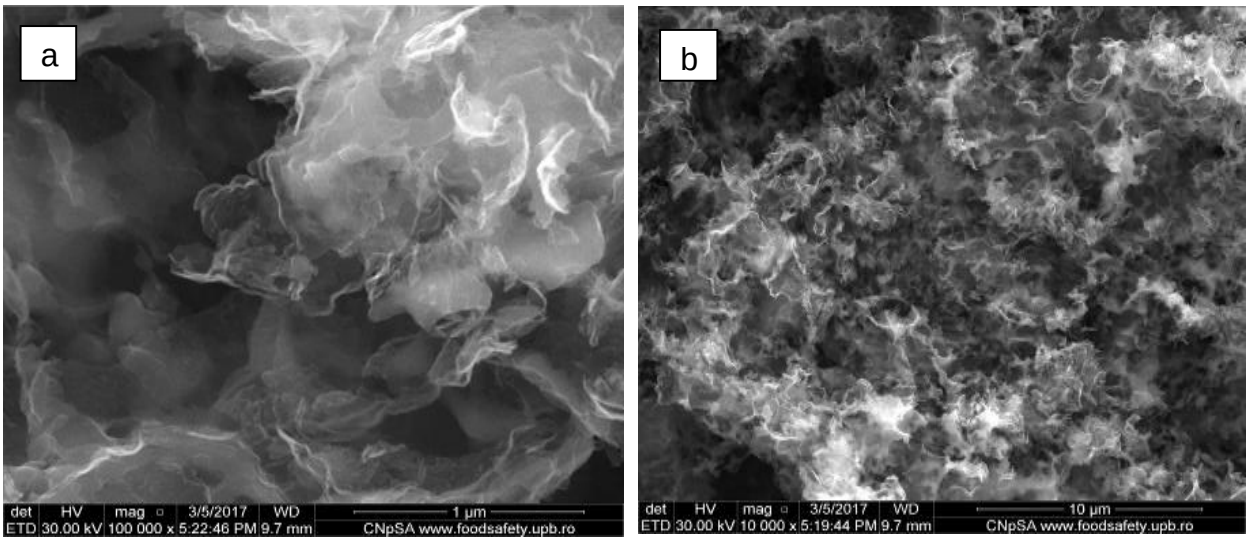

Figure 5.4 SEM images for copper deposit in TiNTs samples.(Figure. 5.4a is for a higher magnification grade than Figure 5.4b.)

5.3.4. ICP-OES investigation

From ICP-OES spectra obtained for solubilized Ti-TiNTsCuNPs sample it can be seen clear peak for Cu at 324.75 nm meaning that new created electrode contains copper. The analytical result using ICP-OES technique for this sample was 0.0038% Cu for entire titanium scrap sample. Analyzed sample weight was 0.4473g.

5.3.5. XRD analyses

Figure 5.5 presents XRD patterns of anodized and annealed titanium scrap sample; it can be observed a small peak at 2θ=25.3° that indicates anatase presence. XRD peaks at 2θ=38° with high intensities are attributed to titanium –which is the substrate for the nanostructured coating.

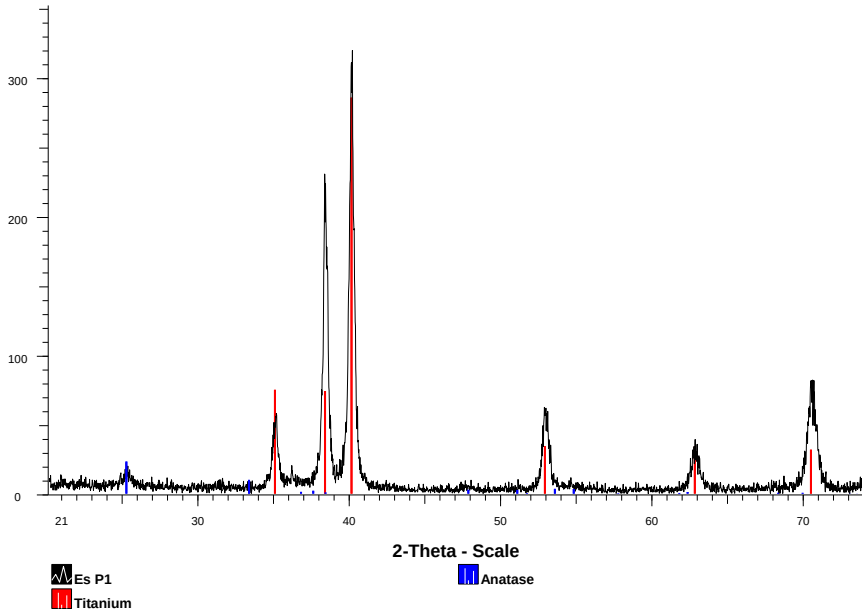

Figure 5.5 XRD patterns of anodized and annealed titanium scrap sample

5.3.6. EIS investigation

Fig. 5.6 presents Bode phase diagram. In this plotting it can be observed modulus linear variation for the both sample (TiNTs and TiNTsCuNPs) on the intermediate and low frequency ranges with a negative slope. This is a characteristic of capacitive behavior. The impedance curve for TiNTsCuNPs sample is shifted to lower values than TiNTs sample impedance plot which means a better electronic conductivity for this sample.Maximum angle phase value is -50° for TiNTs sample and it is reduced to -35° for TiNTsCuNPs sample as it can be seen in Fig.5.6. In this case the phase angle decreases is due to titanium sample support, the new nanoarchitecture built being a thin layer on titanium scrap surface. Even there is not an important impedance drop for TiNTsCuNPS sample compared to TiNTs sample impedance, the photocatalytic properties for the new created electrode were enhanced.

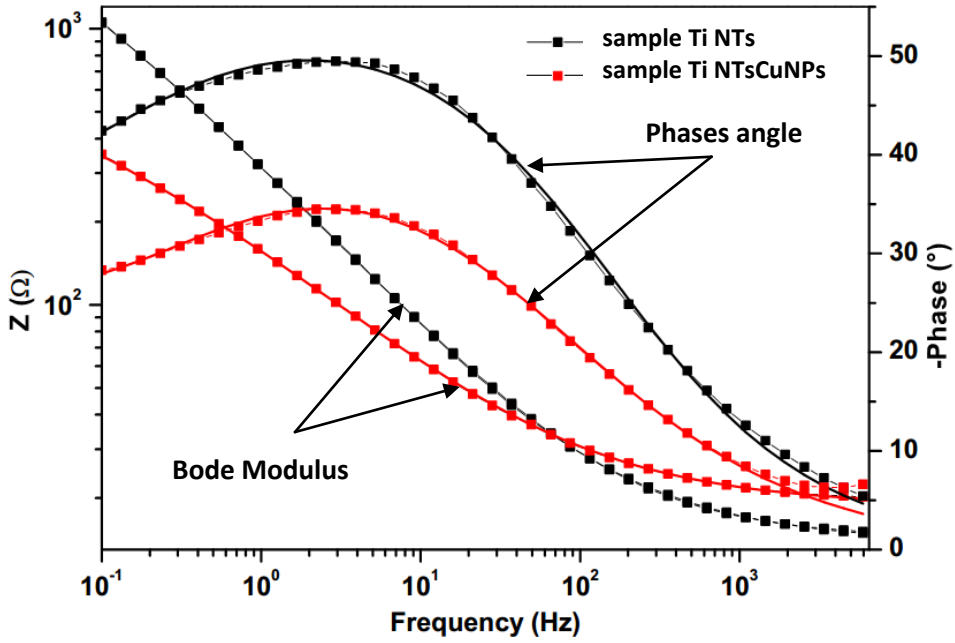

Figure 5.6 Bode phase diagram for TiNTs and TiNTsCuNPs samples.

From Nyquiest diagram presented in Figure 5.7, one can conclude thatTiNTsCuNPs sample presents lower impedance than TiNTs sample meaning a better conductivity.

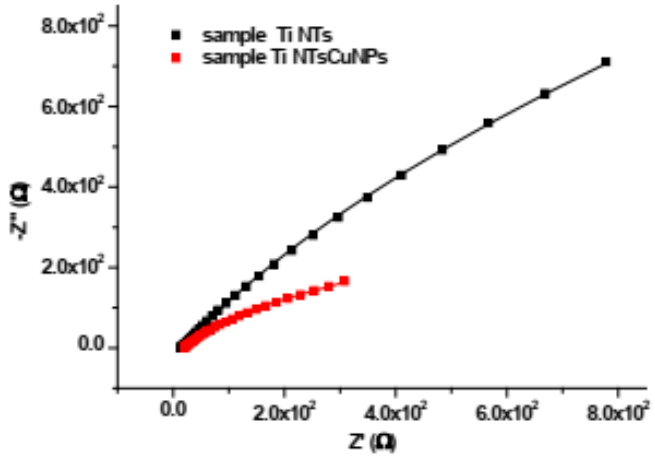

Figure 5.7. Nyquist diagram for TiNTs and TiNTs CuNPs samples

This impedance decreasing is in perfectly accordance with current intensity increasing for the same sample Figure 5.9 (diagrame current-voltage)

The parameters for equivalent circuit are presented and calculated in.. Table… and … Figur

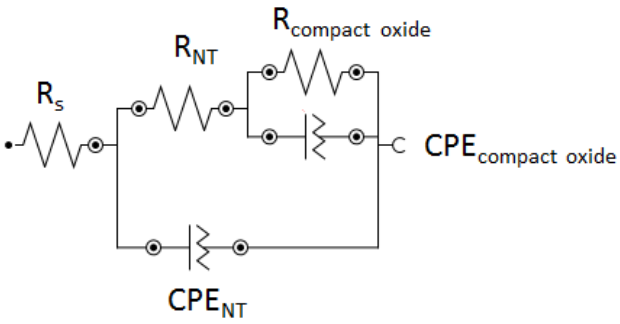

Figure 5.8 Electrical equivalent circuit for TiNTs and TiNTsCuNPs samples.

Probă	$R_s(\Omega)$	$R_{NT}(\Omega)$	$CPE_{NT}(F)$		R_{OCL} (Ω)	$CPE_{OCL}(F)$		χ^2
			$Y_0(S\cdot s^n)$	n		$Y_0(S\cdot s^n)$	n	
TiNTs	14.221	$2.893*10^3$	$9.814*10^{-4}$	0.620	$8.447*10^3$	$18.894*10^{-4}$	0.624	$6.24*10^{-3}$
TiNTsCuNPs	18.696	**$0.547*10^3$**	$21.61*10^{-4}$	0.532	$8.617*10^3$	$88.289*10^{-4}$	0.523	$6.61*10^{-3}$

Table5.1 Parameters for electrical equivalent circuit

In Table 5.1 and Figure 5.8 Rs represent solution resistance, RNT means nanotubes resistance, $R_{compact\ oxide}$ is the resistance of the compact oxide layer, $CPE_{compact\ oxide}$ is the pseudo-capacitance for compact oxide layer and CPENT is the pseudo-capacitance for nanotubes layer. It could be seen in Nyquist diagram (Fig. 10) that the resistance for sample with TiNTsCuNPs decreases in a satisfactory way. The resistance for nanotubes RNT also decreases from 2.893*103 Ω in TiNTs sample to 0.547*103 Ω in TiNTsCuNPs sample meaning a higher current passing through the sample, theoxide layer becoming more conductive and qualifying the new electrode for photocatalytic phenol degradation.

5.3.7. Voltammetry investigation

From the voltammogram presented in Figure5.9, it is noticeable the high current intensity for the TiNTsCuO sample relative to the Ti scrap and TiNTs samples intensity, which explains the new created electrode photocatalytic properties. Current intensities for TiNTs and TiNTsCuNPs sample are very similar, actually they are superposed and difficult to be observed in Figure 5.9. For the investigation was used as electrolyte a solution of Na_2SO_4 0.5M .

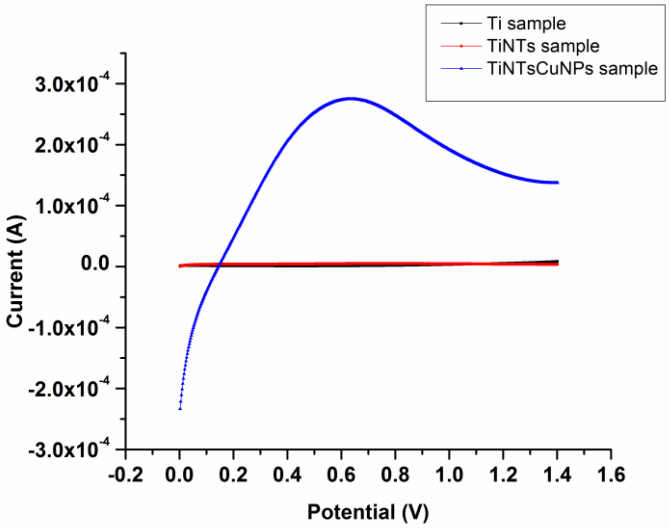

Figure 5.9 Voltammogram for Ti scrap, Ti NTs sample and TiNTsCuO sample

5.3.8. Mott Schottky investigation

Mott Schottky investigation is presented in Figure 5.10 and Table 5.2 lists theflat bad potentials (Fb) and carriers densities (Nd) for TiNTs and TiNTsCuNPs samples in light conditions. From Table 2, flat band potentials are quite close as values while in the case of TiNTsCuNPs sample the value obtained is slightly negatively lower as it was expected. Scientific literature shows that copper doping concentration for TiO2 increases the Fb values becomes more negatively up to -0,55V [43]. Carrier density is higher for TiNTsCuNPs than for TiNTs sample meaning an electrochemical activation which sustains the sample photocatalytic behaviour.

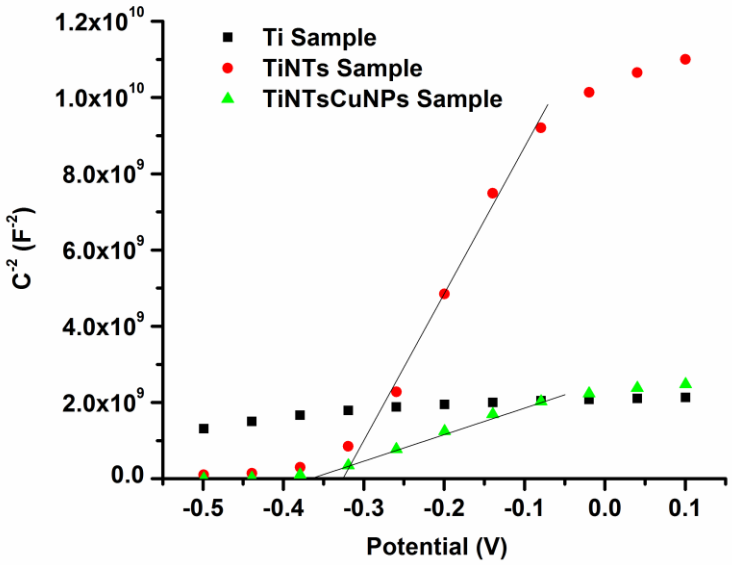

Figure 5.10 mott schottky investigation

Fb(V)	Nd(cm^{-3})	Sample
-0.334	$3.85 \cdot 10^{17}$	TiNTs light
-0.370	$1.97 \cdot 10^{18}$	TiNTsCuNPs light

Table2 Flat band potential (Fb) and carrier density values (Nd) for lighted TiNTs and TiNTsCuO samples.

5.3.9. Phenol degradation

Modified electrodes were used for phenol degradation. LSV investigations were performed for TiNTsCuO sample with phenol solution in order to demonstrate the pollutant degradation. The test realized consists of eight measurements starting from initial moment until to 38 minutes in the same conditions treatment. LSV plotting are presented in Figure 5.11. The experiment was focused on the variation of the current intensity in order to explain the electrochemical processes carried out. Due to the sample with anatase coating that has photocatalytic properties, the created holes generate reactive hydroxyl groups that attack the aromatics nucleus of phenol resulting benzoquinone and hydroquinone. If sufficient hydroxyl radicals are generated, the process is carried out up to maleic acid or oxalic acid and, finally to CO2 and H2O. In our case the degradation due to short testing time the process takes places only up to form benzoquinone and hydrochinone. Cyclic voltammetry studies present a peak potential for benzoquinone at 0.1V and for hydrochinone at 0.5V, these potentials strongly depending on the electrolyte added [44].

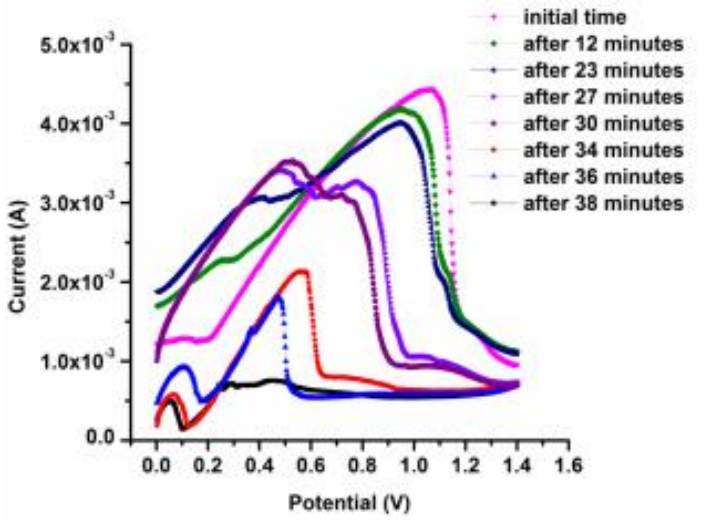

Figure 5.11 Linear sweep voltammetry for TiNTsCuNPs as electrode immersed in an electrolyte of Na_2SO_4 enriched with phenol

In Figure 5.11, which is a plot current (A) vs. potential (V) repeated at different moments is revealed a large peak around 0.9-1V corresponding to the phenol content which is in perfectly agreement to the scientific literature data [45]. It isvery clear that in time two new peaks will appear, one at 0.5V corresponding tohydroquinone and another one at 0-0.2V due to the benzoquinone obtained. Both benzoquinone and hydroquinone are intermediate compounds of phenol degradation. The reaction mechanism is presented in Scheme 5.1.

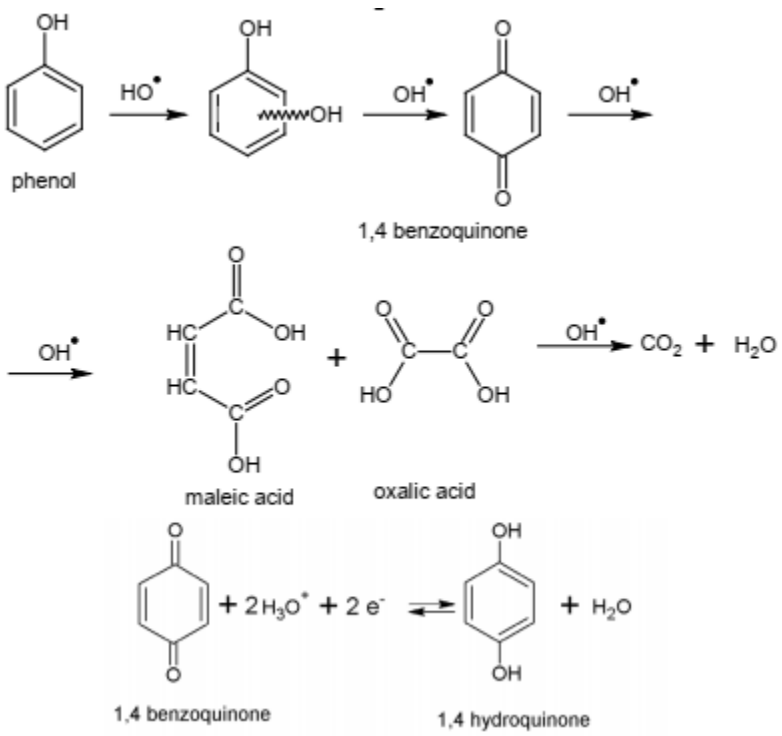

Scheme 5.1 Phenol oxidation reactions/degradation mechanism

It is clear that, the oxidation process is not a totally one up to final oxidation compounds as

it was expected. The explanation could be done by the short time of testing, the irregular shape of the sample and also its roughness that play an important role in nanostructure growing.

5.4. Conclusions

A new electrode was obtained using anodization starting from titanium scrap (waste) provided from a titanium ingots factory in order to obtain a nanostructure of anatase coating on its surface.

Cooper doping used for anatase nanostructure coating enhances material photocatlytic properties in order to support phenol partial degradation, giving the chance for a waste to become a photocatalytic material.

The nano-architecture of new created electrode from titanium scrap was put in evidence by SEM images and proved by ICP-OES technique. Due to the photocatalytic behavior, one possible application of this electrode is in phenol partial degradation in the light conditions.

6. Use of wastes from titanium industry as alternative aggregate for portland cement mortars

6.1. Intoduction

In order to obtain titanium half-finished the titanium ingots are forging. Due to this process there are obtaining a waste coming as a results of shot blasting and polishing with abrasive materials process. This waste is a dusty material which generates a lot of issues meaning storage and their destroying by a specialized company and creates supplementary costs for the titanium ingots.

This waste was divided in two types of material up to their industrial provenience and was named like this:

(DS)- the waste provided by shot blasting ingots processsing

(DSIC)- the waste provided by polishing with abrasive material of titanium forged products

This paper presents some physical and mechanical properties of Portland cement mortars prepared with two types of waste as alternative aggregates.

6.2. Materials and methods

The chemical compositions of DS and DSIC wastes were assessed by inductively coupled plasma optical emission spectrometry (ICP-OES).

The mineralogical composition of the wastes was assessed by X ray diffraction with a Shimadzu XRD 6000 diffractometer. The XRD spectra were obtained using a monochromatic CuKα radiation (λ= 1.5406 Å), range 2θ from 10 to 60 degree.

The microstructure of wastes was assessed with a FEI Inspect F50 High Resolution Scanning Electron Microscopes (SEM) coupled with energy dispersive X ray spectroscopy (EDX).

The SEM analyses were performed in fracture of specimens (without metal coating).

Due to the wide grain size distribution of DSIC waste this material was first separated by sieving in three fractions: DSICf – fraction below 400 microns, DSICm – fraction with grain size in the range 400 microns and 2 mm and DSICg- fraction with grains bigger than 2 mm. The amount of each fraction was: DSICf - 25%, DSICm - 48%, DSICg - 27%. The chemical composition of these three fractions, assessed by ICP-OES is presented in Table 6.1

Specimen	Fr<0.15mm (g)			Fr.0.15-0.5mm (g)			Fr. 0.5-1mm (g)		
	Sand	DSIC	DS	Sand	DSIC	DS	Sand	DSIC	DS
N	150	-	-	300	-	-	450	-	-
DSIC	-	150	-	-	300	-	-	450	-
N-DS	-	-	150	-	-	300	-	-	450
DSIC-DS	-	-	150	-	-	300	-	450	-

Table 6.1 Composition of aggregates (g) used for Portland cement mortars preparation

DS and DSIC wastes replaced various fractions in the composition of standard aggregate (sand - SR EN 196-1/ 2006, used for Portland cement mortar preparation – see Table 6.1.

The mortar specimens were prepared with a cement to aggregate ratio of 1/3 and water to cement ratio of 0.5. The mortar specimens were prepared in accordance with the SR EN 196-1 norm; the fresh mortar was cast in rectangular molds (40x40x160mm) and vibrated for 2 minutes. The specimens were cured in the mold (covered with cling film) at room temperature the first 24 hours, then de-molded and immersed in water (20±2 ºC) up to 28 days. The following

characteristics were assessed on mortar specimens cured 3 or 28 days: apparent density, compressive and flexural strengths. The density of sand, DS and DSIC wastes was assessed with a helium pycnometer-Pycnomatic ATC.

6.3. Results and discussions

6.3.1. Characterization of DS and DSIC wastes

The DS and DSIC wastes are granular materials. As it can be seen in Figure 6.1, DS waste is more homogenous and contains smaller grains opposite to DSIC waste which contains a high amount of coarse grains.

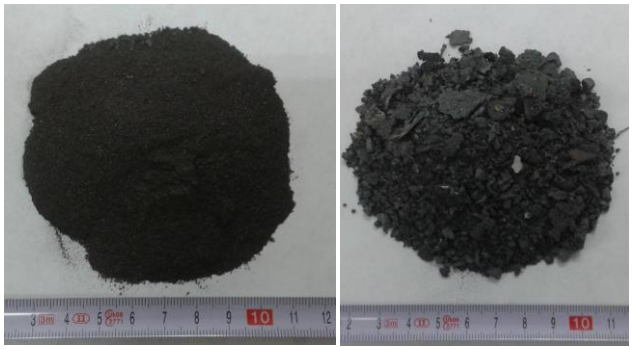

Figure 6.1 - Visual aspects of wastes: DS (a) and DSIC (b)

This is connected with the mechanical processing in which these two wastes result: DS - results by the shot blasting (with steel beads) of titanium ingots and DSIC results during the surface abrasion/polishing process with abrasive discs of Ti ingots.

The density, assessed with a helium-pycnometer is 6928 kg/m3 for DS waste and 4217 kg/m3 for DSIC waste. Both wastes have higher densities as compared with quartz sand i.e. 2070 kg/m3.

The chemical composition of DS waste (filtrate and melt) assessed by ICP-OES is presented in Table 6.2. One can notice the high amount of iron (86.56%) – determined by the presence of steel beads remains. The Ti content is 8.23% and is higher in the melt as compared with filtrate solution.

Element (%)	Filtrate	Topitură	Total
Al	0.49	0.64	1.13
Cr	0.31	-	0.31
Cu	0.26	-	0.26
Fe	86.26	0.3	86.56
Mn	0.005	-	0.005
Mo	0.005	-	0.005
Ni	0.12	-	0.12
Si	0.24	0.36	0.6
Ti	2.38	5.85	8.23
V	0.1	0.17	0.27
Zn	0.005	-	0.005
C*	0.9		
Total (%)	98.39		

*) C was determined with an automatic gas –analyzer

Table 6.2 Chemical composition of DS waste

Due to the wide grain size distribution of DSIC waste this material was first separated by sieving in three fractions: DSICf – fraction below 400 microns, DSICm – fraction with grain size in the range 400 microns and 2 mm and DSICg- fraction with grains bigger than 2 mm. The amount of each fraction was: DSICf - 25%, DSICm - 48%, DSICg - 27%. The chemical composition of these three fractions, assessed by ICP-OES is presented in Table 6.3.

Element (%)	DSICf			DSICm			DSICg			DSIC Media
	Filtrate	Melt	Total	Filtrate	Melt	Total	Filtrate	Melt	Total	
Al	1.38	6.48	7.86	0.57	15.3	15.87	0.38	11.6	11.98	12.817
Cd	0.005	0	0.005	0.005	0	0.005	0.005	0	0.005	0.005
Cr	0.012	0	0.012	0	0	0	0	0	0	0.003
Fe	2.5	0.14	2.64	1.42	0.39	1.81	0.13	0.8	0.93	1.7799
Mn	0.055	0	0.055	0.032	0	0.032	0.008	0	0.008	0.0313
Ni	0.006	0	0.006	0.005	0	0.005	0.005	0	0.005	0.0053
Pb	0.005	0	0.005	0.005	0	0.005	0.005	0	0.005	0.005
Si	0.18	1.19	1.37	0.085	0.93	1.015	0.039	1.24	1.279	1.175
Ti	17.82	42.12	59.94	29.4	5.6	35	2.22	45.1	47.32	44.561
V	0.94	1.21	2.15	0.33	1.02	1.35	0.22	0.8	1.02	1.4609
Zn	0.012	0.012	0.024	0	0	0	0	0	0	0.006
C	1.6			1.15			0.6			1.114
Total (%)										62.964*

*) The difference up to 100% is due to the oxygen or/and nitrides

Table 6.3 Chemical composition of DSIC waste

As it can be seen in the Table 6.3, DSIC waste has a high amount of titanium (44.561%) and this element is distributed in all three grain size fractions. Also the Al content in this waste is important – 12.817%.

The mineralogical composition of DS and DSIC wastes was assessed by XRD – Figures 6.2 and 6.3.

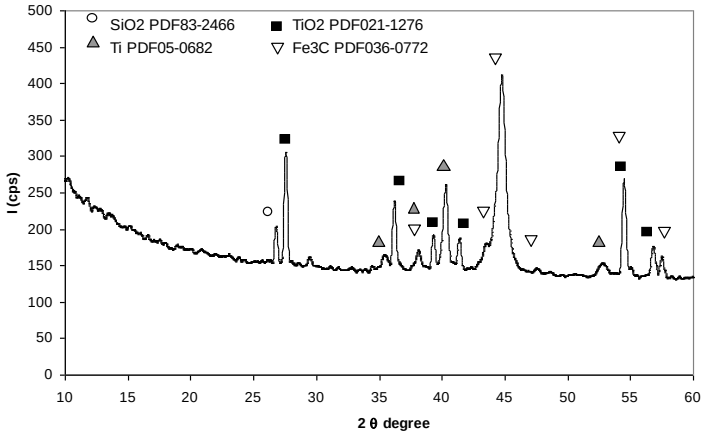

Figure 6.2 XRD spectra of DS waste

As it can be seen in Figure 2, the main phases assessed by XRD in DS waste are iron carbide (Fe3C) - compound present in steel beads, metallic titanium and titanium oxide –resulted due to

the superficial oxidation of Ti ingot.

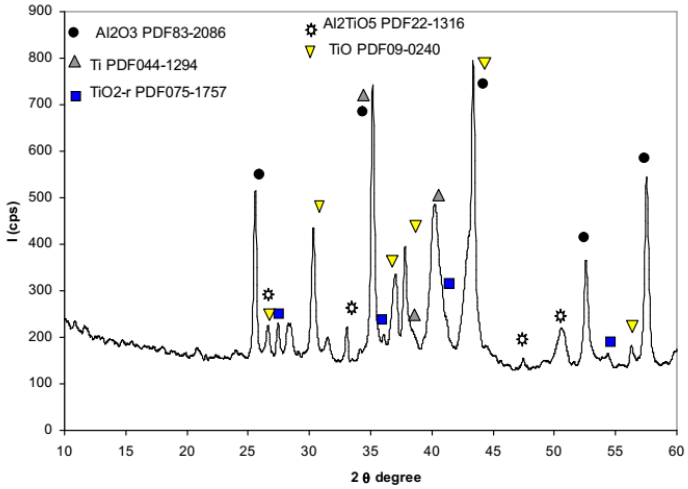

Figure 6.3 XRD spectra of DSIC waste

The main compounds assessed by XRD in DSIC waste (Figure 6.3) are metallic Ti, titanium oxides (TiO and TiO2); Al is also present in this waste (see Table 6.3) as Al2O3 and AlTiO5

The microstructure of DS and DSIC wastes was assessed by scanning electron microscopy (SEM) and the elemental composition of phases was analyzed by EDX, Figure 6.4, 6.5 și 6.6.

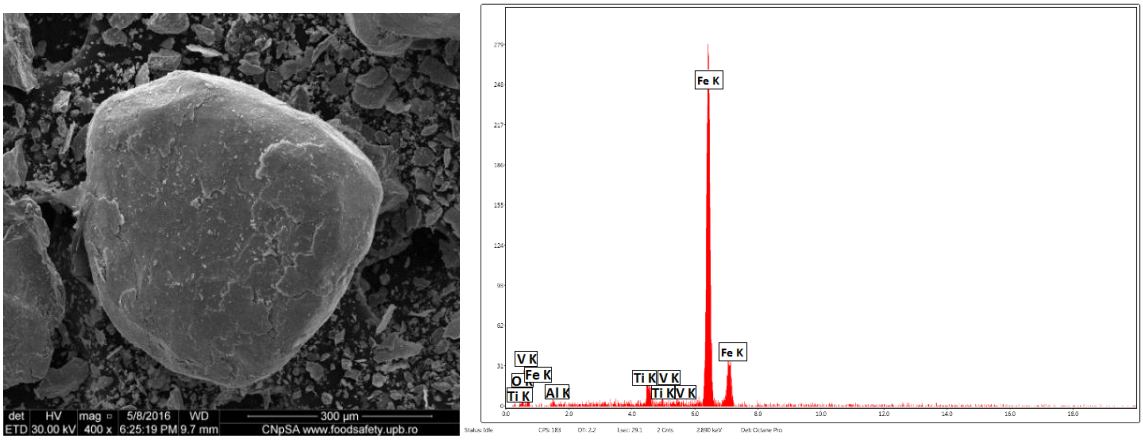

Figure 6.4 SEM micrograph and corresponding EDX spectra for DS waste

As it can be seen in Figure 4, DS waste consists of grains with various forms (plates, polyhedral and irregular shapes. The EDX spectra show the presence of iron (in high quantity) along with small quantities of titanium, aluminium and vanadium.

DSIC waste consists mainly in big agglomerations of smaller grains (Figure 6.5). One can also assess solidified melt (see arrows in Fig. 6.5) that contributes to the aggregate formation.

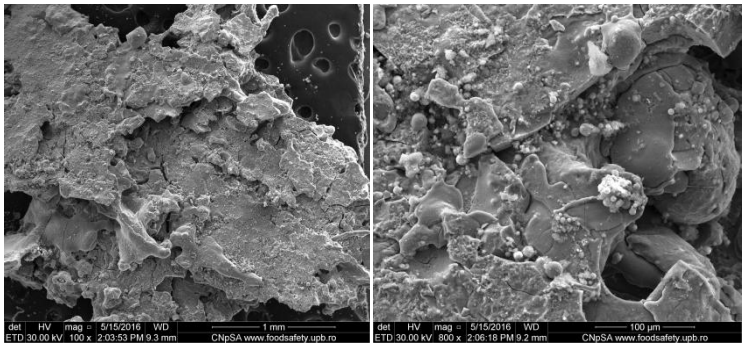

Figure 6.5 SEM micrograph for DSIC waste

From Figure 6.6 it can be seen that titanium is main element assessed by EDX analysis in DSIC waste. One can also observe hollow of porous microspheres (Figure 6.6) formed due to the partial melting of titanium alloy during its processing.

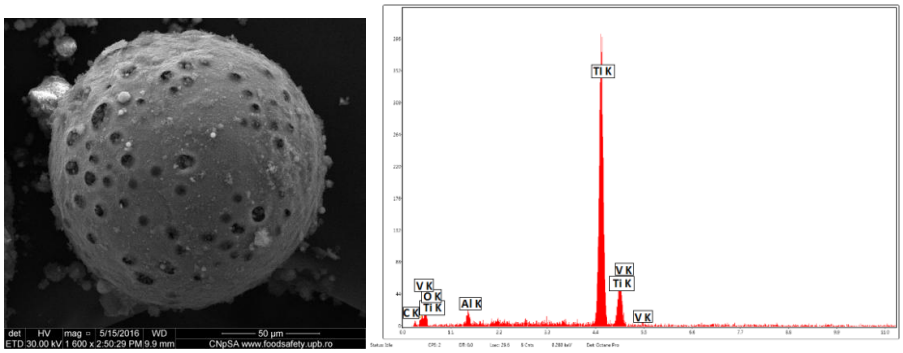

Figure 6.6 SEM micrograph and corresponding EDX spectra for DSIC waste

6.3.2. Properties of Portland cement mortars with DS and DSIC as alternative aggregates

The apparent density of mortar specimens prepared with various dosages of sand, DS and DSIC (see Table 1) is presented in Figure 6.7

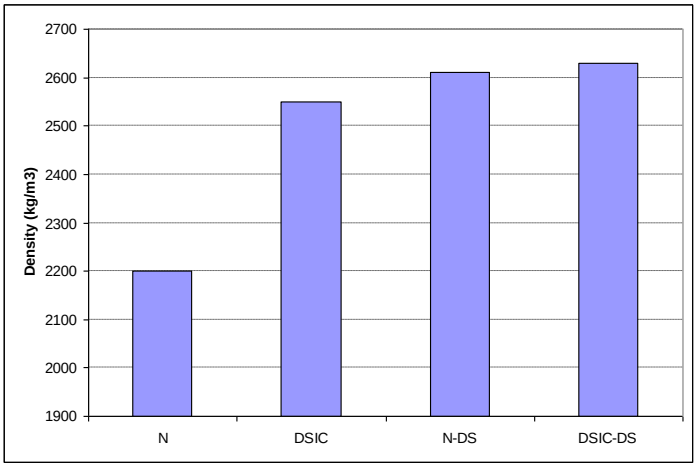

Figure 6.7 Apparent density of cement mortar specimens with different types of aggregates

As it can be seen, the mortar specimens in which sand aggregate was replaced totally or partially with various amounts of DS and DSIC waste have higher densities as compared with reference (N). This increase of density values, especially for the mortars with DS waste is in good correlation with the high values assessed for the densities of studied wastes i.e. 6982 kg/m3 for DS and 4217 kg/m3 for DSIC.

The values of flexural and compressive strengths assessed on mortar specimens are presented in Figure 6.8. Both flexural and compressive strengths increase when sand is totally replaced with DSIC waste. That was to be expected, due to the high amount of titanium alloy grains (with high hardness) present in this waste. The partial replacement of sand (N) and DSIC with DS waste has a negative influence on the mechanical strengths of mortars; N-DS mortars have lower values of flexural and compressive strengths both at early ages (3 days) and longer hardening times (28 days). The negative effect determined by DS waste on the mechanical strengths of mortar specimens is also connected with its grain size and chemical composition i.e. coarse grains with high iron content.

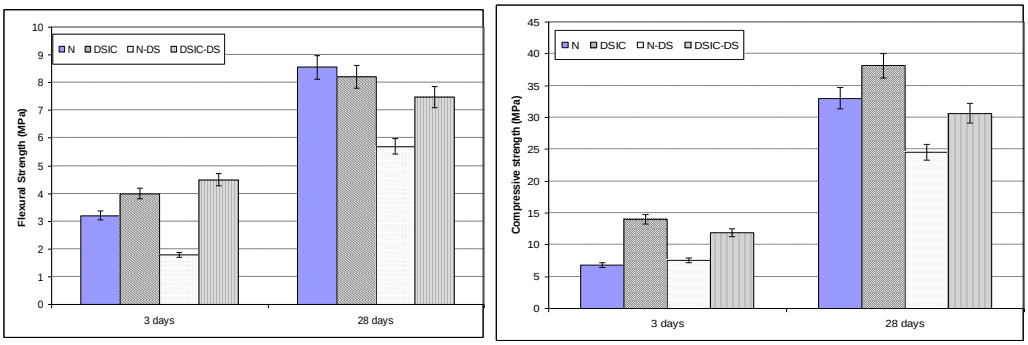

Figure 6.8 Flexural (a) and compressive (b) strengths assessed on mortar specimens with DS and DSIC wastes, hardened for 3 and 28 days

7. Conclusions

The DS and DSIC wastes resulted in titanium alloy mechanical processing (shot blasting or polishing) can be used to substitute the natural aggregate (sand) in the manufacture of Portland cement mortars, as alternative aggregates.

The chemical and mineralogical compositions as well as the grain size distribution of DS and DSIC wastes are influenced by the mechanical process in which are generated. DS, which results by the shot blasting with steel beads, has a high amount of Fe (86.56%) and a smaller Ti content (8.23%).

DSIC, which results during the surface abrasion/polishing process with abrasive discs of Ti ingots, has a high Ti (44.56%) and Al (12.81%) content; in this waste Ti is present as metal as well as titanium oxides (in smaller quantities).

The apparent densities of Portland cement mortars containing DS and DSIC as alternative aggregate are higher as compared with the reference mortar (prepared with sand), due to the higher density of these wastes.

The total replacement of sand with DSIC in mortar determines an increase of mechanical strengths both at early ages (3 days) and longer hardening times (28 days).

The mortar specimens with DS waste developed lower flexural and compressive strengths as compared with the reference and the mortar with DSIC as alternative aggregate.

8. References

1. Aeimbhu, A., *Scanning Electron Microscope for Characterising of Micro- and Nanostructured Titanium Surfaces* Scanning Electron Microscopy, 2012.
2. Ijadpanah-saravi, H., et al., *Synthesis of Titanium Dioxide Nanoparticles for Photocatalytic Degradation of Cyanide in Wastewater.* Analytical Letters, 2014. **47**: p. 1772-1782.
3. M.E. Fitzpatrick1, A.T.F., P. Holdway3, F.A. Kandil2, J. Shackleton4 and L. Suominen51 Open University, 2 National Physical Laboratory, 3 QinetiQ. *Determination of Residual Stresses by X-ray Diffraction* 2005 Available from: www.npl.co.uk.
4. Ben O'Sullivan*, S.G. *Plain Radiograph/X-ray*. 2017; Available from: https://www.insideradiology.com.au/plain-radiograph-x-ray/.
5. Giuliani, A., et al., *High-Resolution X-Ray Tomography: A 3D Exploration Into the Skeletal Architecture in Mouse Models Submitted to Microgravity Constraints.* 2018. **9**(181).
6. Sahoo, B.N., B. Kandasubramanian, and A. Thomas, *Effect of TiO₂ Powder on the Surface Morphology of Micro/Nanoporous Structured Hydrophobic Fluoropolymer Based Composite Material.* Journal of Polymers, 2013. **2013**: p. 615045.
7. Zhang, M., et al., *Lotus effect in wetting and self-cleaning.* Biotribology, 2016. **5**: p. 31-43.
8. Horiba. *The most common domains of applications for ICP-OES*. 2020; Available from: https://www.horiba.com/en_en/applications-icp-oes.
9. Saleh, T.A. and V.K. Gupta, *Photo-catalyzed degradation of hazardous dye methyl orange by use of a composite catalyst consisting of multi-walled carbon nanotubes and titanium dioxide.* Journal of Colloid and Interface Science, 2012. **371**(1): p. 101-106.
10. Chen, S., et al., *Synergistic antibacterial mechanism and coating application of copper/titanium dioxide nanoparticles.* Chemical Engineering Journal, 2014. **256**: p. 238-246.
11. Déléris, G. and C. Petibois, *Applications of FT-IR spectrometry to plasma contents analysis and monitoring.* Vibrational Spectroscopy, 2003. **32**(1): p. 129-136.
12. Petibois, C. and G. Déléris, *Oxidative stress effects on erythrocytes determined by FT-IR spectrometry.* Analyst, 2004. **129**(10): p. 912-916.
13. Polshin, E., et al., *Beer quality screening by FT-IR spectrometry: Impact of measurement strategies, data pre-processings and variable selection algorithms.* Journal of Food Engineering, 2011. **106**(3): p. 188-198.
14. Guskos, N., et al., *EPR, spectroscopic and photocatalytic properties of N-modified TiO2 prepared by different annealing and water-rinsing processes.* Materials Chemistry and Physics, 2012. **136**: p. 889-896.
15. Behnajady, M., S. Yavari, and N. Modirshahla, *Investigation on adsorption capacity of TiO2-P25 nanoparticles in the removal of a mono-azo dye from aqueous solution: A comprehensive isotherm analysis.* Chemical Industry and Chemical Engineering Quarterly, 2014. **20**: p. 97-107.
16. Das, P., et al., *Insight into adsorption equilibrium, kinetics and thermodynamics of Malachite Green onto clayey soil of Indian origin.* Chemical Engineering Journal - CHEM ENG J, 2010. **165**: p. 874-882.
17. Viswanathan, B. and K.R. Krishanmurthy, *Nitrogen Incorporation in TiO2: Does It Make a Visible Light Photo-Active Material?* International Journal of Photoenergy, 2012. **2012**: p. 1-10.

18. Klosek, S. and D. Raftery, *Visible Light Driven V-Doped TiO2 Photocatalyst and Its Photooxidation of Ethanol.* The Journal of Physical Chemistry B, 2001. **105**(14): p. 2815-2819.
19. Ungureanu, C., et al., *Enhancing antimicrobial activity of TiO2/Ti by torularhodin bioinspired surface modification.* Bioelectrochemistry, 2016. **107**: p. 14-24.
20. Ungureanu, C. and M. Ferdes, *Evaluation of Antioxidant and Antimicrobial Activities of Torularhodin.* Advanced Science Letters, 2012. **18**(1): p. 50-53.
21. Pan, J., et al., *Photoinduced Electron Transfer between a Carotenoid and TiO2 Nanoparticle.* Journal of the American Chemical Society, 2002. **124**(46): p. 13949-13957.
22. Jaiswal, S., et al., *Enhancement of the antibacterial properties of silver nanoparticles using beta-cyclodextrin as a capping agent.* Int J Antimicrob Agents, 2010. **36**(3): p. 280-3.
23. Hanaor, D.A.H. and C.C. Sorrell, *Review of the anatase to rutile phase transformation.* Journal of Materials Science, 2010. **46**(4): p. 855-874.
24. Teodorescu-Soare, C.T., et al., *Growth and characterization of TiO2 nanotube arrays under dynamic anodization. Photocatalytic activity.* Journal of Electroanalytical Chemistry, 2018. **823**: p. 388-396.
25. Mustapha, S., et al., *Application of TiO2 and ZnO nanoparticles immobilized on clay in wastewater treatment: a review.* Applied Water Science, 2020. **10**(1).
26. Shaban, M., A.M. Ashraf, and M.R. Abukhadra, *TiO2 Nanoribbons/Carbon Nanotubes Composite with Enhanced Photocatalytic Activity; Fabrication, Characterization, and Application.* Sci Rep, 2018. **8**(1): p. 781.
27. Vu, T.H.T., et al., *Synthesis of titanium dioxide nanotubes via one-step dynamic hydrothermal process.* Journal of Materials Science, 2014. **49**(16): p. 5617-5625.
28. Viana, B.C., et al., *Decorating Titanate Nanotubes with CeO2 Nanoparticles.* The Journal of Physical Chemistry C, 2009. **113**(47): p. 20234-20239.
29. Dumitriu, C., et al., *Ti surface modification with a natural antioxidant and antimicrobial agent.* Surface and Coatings Technology, 2015. **276**: p. 175-185.
30. Qu, Q., et al., *Chemically Binding Carboxylic Acids onto TiO2 Nanoparticles with Adjustable Coverage by Solvothermal Strategy.* Langmuir, 2010. **26**(12): p. 9539-9546.
31. León, A., et al., *FTIR and Raman Characterization of TiO2 Nanoparticles Coated with Polyethylene Glycol as Carrier for 2-Methoxyestradiol.* Applied Sciences, 2017. **7**(1).
32. Ramos Hernández, J., et al., *Use of Electrosprayed Agave Fructans as Nanoencapsulating Hydrocolloids for Bioactives.* Nanomaterials, 2018. **8**: p. 868.
33. Haiyee, Z.A., M.N.A.A. Marhanna, and M.A.J.i.f.r.j. Atirah, *Characterisation and solubility study of ³-cyclodextrin and#²-carotene complex.* 2011. **18**: p. 1061-1065.
34. Lozano-Navarro, J.I., et al., *Chitosan-Starch Films with Natural Extracts: Physical, Chemical, Morphological and Thermal Properties.* Materials (Basel, Switzerland), 2018. **11**(1): p. 120.
35. Ibukun, O. and H.K. Jeong, *Enhancement of photocatalytic activities of nitrogen-doped titanium dioxide by ambient plasma.* Chemical Physics Letters, 2020. **744**: p. 137234.
36. Radecka, M., et al., *Importance of the band gap energy and flat band potential for application of modified TiO2 photoanodes in water photolysis.* Journal of Power Sources, 2008. **181**(1): p. 46-55.

37. Matsunaga, T., et al., *Photoelectrochemical sterilization of microbial cells by semiconductor powders.* FEMS Microbiology Letters, 1985. **29**(1): p. 211-214.
38. Matsunaga, T., et al., *Continuous-sterilization system that uses photosemiconductor powders.* 1988. **54**(6): p. 1330-1333.
39. Luttrell, T., et al., *Why is anatase a better photocatalyst than rutile?--Model studies on epitaxial TiO2 films.* Sci Rep, 2014. **4**: p. 4043.
40. Aguilar, T., et al., *A route for the synthesis of Cu-doped TiO2 nanoparticles with a very low band gap.* Chemical Physics Letters, 2013. **571**: p. 49-53.
41. Dumitriu, C., et al., *Antibacterial efficiencies of TiO2 nanostructured layers prepared in organic viscous electrolytes.* Applied Surface Science, 2015. **341**: p. 157-165.
42. Rosenbaum, J., et al., *Antibacterial properties of nanostructured Cu-TiO2 surfaces for dental implants.* Biomater Sci, 2017. **5**(3): p. 455-462.
43. Wijayarathna, T.R., et al., *A high efficiency indoline-sensitized solar cell based on a nanocrystalline TiO(2) surface doped with copper.* Nanotechnology, 2008. **19**(48): p. 485703.
44. Quan, M., et al., *Voltammetry of quinones in unbuffered aqueous solution: reassessing the roles of proton transfer and hydrogen bonding in the aqueous electrochemistry of quinones.* J Am Chem Soc, 2007. **129**(42): p. 12847-56.
45. Uskova, I.K. and O.N. Bulgakova, *Cyclic voltammetry of phenol.* Journal of Analytical Chemistry, 2014. **69**(6): p. 542-547.